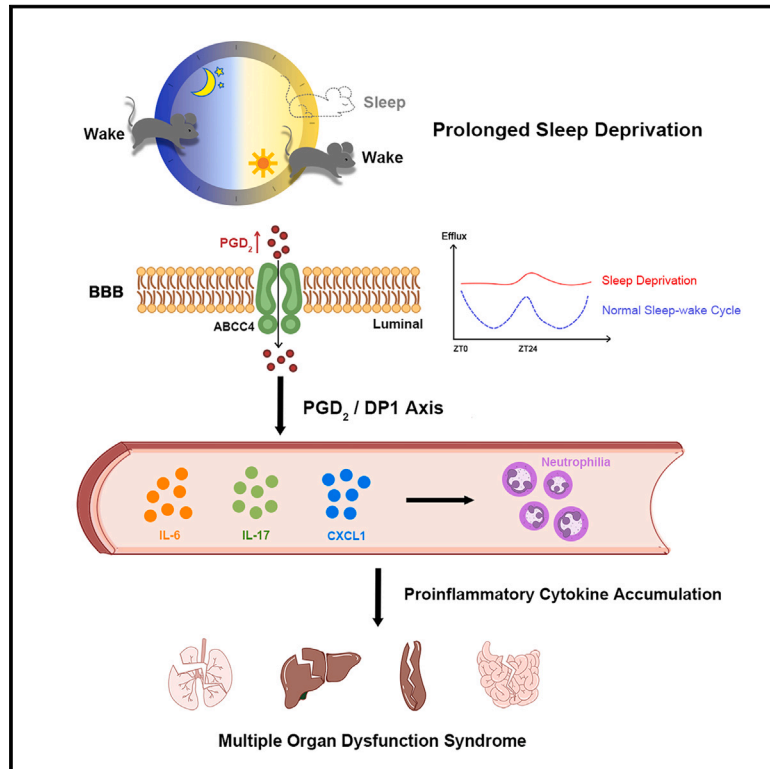


Prolonged sleep deprivation induces a cytokine-storm-like syndrome in mammals

Graphical abstract



Authors

Di Sang, Keteng Lin, Yini Yang, ..., Qinghua Liu, Yulong Li, Eric Erquan Zhang

Correspondence

zhangerquan@nibs.ac.cn

In brief

Enhanced efflux of PGD_2 across the BBB during prolonged sleep deprivation induces a cytokine-storm-like syndrome via the $\text{PGD}_2/\text{DP1}$ axis. Sleep deprivation in mice that involves disruption of REMS and NREMS leads to lethality due to brain prostaglandin D_2 -mediated cytokine-storm-like systemic inflammation.

Highlights

- A highly efficient paradigm is introduced for depriving mice of sleep
- PGD_2 efflux across the BBB is enhanced by sleep deprivation
- Sleep deprivation triggers increases in both cytokines and circulating neutrophils
- The sleep-deprived brain affects the peripheral immune system via the $\text{PGD}_2/\text{DP1}$ axis



Article

Prolonged sleep deprivation induces a cytokine-storm-like syndrome in mammals

Di Sang,^{1,2,14} Keteng Lin,^{2,3,14} Yini Yang,^{4,14} Guangdi Ran,^{2,5} Bohan Li,^{6,7} Chen Chen,² Qi Li,^{2,5} Yan Ma,^{2,5} Lihui Lu,² Xi-Yang Cui,⁸ Zhibo Liu,^{6,8} Sheng-Qing Lv,⁹ Minmin Luo,^{2,10,11} Qinghua Liu,^{2,5} Yulong Li,^{4,6,12,13} and Eric Erquan Zhang^{2,5,15,*}

¹Graduate School of Peking Union Medical College, Chinese Academy of Medical Sciences, Beijing, China

²National Institute of Biological Sciences, Beijing, China

³College of Biological Sciences, China Agricultural University, Beijing, China

⁴Peking University School of Life Sciences, Beijing, China

⁵Tsinghua Institute of Multidisciplinary Biomedical Research, Tsinghua University, Beijing, China

⁶Peking-Tsinghua Center for Life Sciences, Beijing, China

⁷Academy for Advanced Interdisciplinary Studies, Peking University, Beijing, China

⁸Beijing National Laboratory for Molecular Sciences, Radiochemistry and Radiation Chemistry Key Laboratory of Fundamental Science

College of Chemistry and Molecular Engineering, Peking University, Beijing, China

⁹Department of Neurosurgery, Xinqiao Hospital, Chongqing, China

¹⁰School of Life Sciences, Tsinghua University, Beijing, China

¹¹Chinese Institute for Brain Research, Beijing, China

¹²State Key Laboratory of Membrane Biology, Beijing, China

¹³PKU-IDG/McGovern Institute for Brain Research, Beijing, China

¹⁴These authors contributed equally

¹⁵Lead contact

*Correspondence: zhangerquan@nibs.ac.cn

<https://doi.org/10.1016/j.cell.2023.10.025>

SUMMARY

Most animals require sleep, and sleep loss induces serious pathophysiological consequences, including death. Previous experimental approaches for investigating sleep impacts in mice have been unable to persistently deprive animals of both rapid eye movement sleep (REMS) and non-rapid eye movement sleep (NREMS). Here, we report a “curling prevention by water” paradigm wherein mice remain awake 96% of the time. After 4 days of exposure, mice exhibit severe inflammation, and approximately 80% die. Sleep deprivation increases levels of prostaglandin D₂ (PGD₂) in the brain, and we found that elevated PGD₂ efflux across the blood-brain-barrier—mediated by ATP-binding cassette subfamily C4 transporter—induces both accumulation of circulating neutrophils and a cytokine-storm-like syndrome. Experimental disruption of the PGD₂/DP1 axis dramatically reduced sleep-deprivation-induced inflammation. Thus, our study reveals that sleep-related changes in PGD₂ in the central nervous system drive profound pathological consequences in the peripheral immune system.

INTRODUCTION

Sleep is indispensable for most animals.^{1,2} Humans spend nearly one-third of their lives asleep, but the precise function and mechanism of sleep remain controversial.³ Sleep is critically involved in numerous biological processes, including immune regulation,⁴ cognitive performance,⁵ and metabolism.⁶ Extended sleep deprivation (SD) can lead to premature mortality in a range of model animals (e.g., flies,^{7,8} cockroaches,⁹ mice,¹⁰ rats,^{11,12} and dogs¹³), and it has been suggested that sleep-loss-induced mortality is driven by the accumulation of reactive oxygen species (ROS) in the gut.⁸ Numerous health problems result from insufficient sleep,^{14,15} including, but not limited to, increased susceptibility to infection,¹⁶ chronic inflammatory dis-

eases,^{14,17} and inflammation.¹⁸ Sleep loss has also been linked to improper clearance of metabolites and proteins from the central nervous system (CNS),¹⁹ the production of cytokines (e.g., interleukin [IL]-1 and tumor necrosis factor) in the CNS,²⁰ and oxidative stress.^{8,21} However, the detailed mechanisms by which sleep regulates immunity and how insufficient sleep results in adverse health effects have not been elucidated.

Experimental manipulation of sleep duration provides a reliable measure for dissecting how sleep regulates innate immunity in both human and animal models.²² Manipulations of sleep duration include total SD, chronic sleep restriction, and sleep disruption.²³ In laboratory experiments, total SD is the most commonly used sleep manipulation,²³ and many SD paradigms have been developed in mice. These include gentle handling,²⁴

moving treadmills,²⁵ rotating wheels,²⁵ and multiple platforms over water.^{26,27} However, these conventional SD paradigms do not efficiently suppress all sleep for long periods of time, as animals have a homeostatic mechanism that drives robust recovery after an initial loss of sleep.^{28–30} Thus, a more efficient experimental paradigm for inducing prolonged and continuous SD is necessary to rigorously explore the function of sleep.

Here, we report a modified SD paradigm for mice that we call “curling prevention by water” (CPW), which resembles the previously reported disk-over-water (DOW) paradigm for rats. The CPW paradigm dramatically depleted mice of both rapid eye movement sleep (REMS) and non-rapid eye movement sleep (NREMS) over a long timescale (>4 days). As a consequence of this prolonged SD, mice exhibited severe systemic inflammation and premature mortality. The systemic inflammation seen during SD was characterized by cytokine-storm-like symptoms with multiple organ dysfunction syndrome (MODS), upregulation of multiple proinflammatory cytokines, and accumulation of circulating neutrophils. These immune consequences were caused by the enhanced efflux of prostaglandin (PG) D₂ (PGD₂) across the brain-blood barrier (BBB) through ATP-binding cassette (ABC) subfamily C4 transporter (ABCC4). Blocking this PGD₂/PGD₂ receptor 1 (DP1) axis, either pharmacologically or genetically, dramatically reduced SD-induced inflammation.

RESULTS

A paradigm for inducing prolonged SD in mice

To develop an efficient SD paradigm, we analyzed extensive video recordings of mouse sleep/wake cycles over prolonged durations. These ethological analyses revealed that mice adopt a curled-up position with lowered heads when they enter the sleep state. Drawing inspiration from the DOW paradigm, which involves monitoring SD rats via electroencephalogram/electromyogram (EEG/EMG),¹¹ we postulated that placing mice in a shallow layer of water could prevent sleep. This concept led to the inception of the CPW paradigm (or SD, as referred to subsequently). Succinctly, mice subjected to the CPW paradigm are housed in a cage that contain a shallow layer of water (~8 mm deep), which just reaches their ankles (Figure 1A). As the mice exhibit signs of falling asleep, characterized by body curling, they are promptly awakened as their noses touch the water.

To evaluate the efficiency of the CPW paradigm in preventing sleep, we conducted EEG/EMG-based sleep/wake analysis on adult C57BL/6J mice (Figure S1A). On average, mice exposed to CPW remained awake for ~1,400 min/day, constituting 96% of the total time (Figures 1B and 1C). On average, this resulted in the deprivation of ~95% (545 min/day) of NREMS and ~83% (54 min/day) of REMS compared with home-cage controls (Figures 1D and S1B–S1D). Thus, the efficiency of the CPW paradigm was comparable with, if not superior to, the well-established DOW paradigm in rats¹¹ (Figure S1F).

Acute SD triggers a substantial rebound in sleep due to sleep homeostasis mechanisms.^{28–30} To determine if mice displayed normal sleep recovery (SR) following CPW-induced SD, we subjected them to 8 h of SD followed by 16 h of recovery (Figure S1G). During this recovery phase, mice exhibited significantly increased amounts of both NREMS and REMS compared

with baseline recordings. This led to the recovery of ~160 min of NREMS (56% of NREMS lost during CPW) and ~50 min of REMS (98% of REMS lost during CPW) (Figures S1H and S1I). Taken together, these findings consistently demonstrate that the CPW paradigm effectively prevents sleep in mice.

The water layer associated with the CPW paradigm creates a humid environment. To investigate the impact of this humidity on sleep in mice, we placed a wet, gauze-covered platform in the CPW paradigm setup to create an environmental control (eCon) condition (Figure 1A). Comparatively, eCon mice experienced only a minimal loss of sleep per day (99 min or 16%) compared with the home-cage controls (Figure 1C). Notably, this augmented wakefulness was observed primarily during the Zeitgeber Time (ZT)0~ZT1 period and was associated with the daily cage switch (Figures 1C, 1D, and S1E). Thus, differences between CPW-subjected and control mice can be attributed to SD, rather than the humid environment.

To assess whether the CPW paradigm induces more stress than other SD paradigms, we compared CPW-subjected mice with those subjected to a commercially available stand-alone SD (SASD) paradigm,⁸ where a sweeping bar continuously pushes the mice to disrupt their sleep. CPW- and SASD-subjected mice had comparable serum levels of the stress hormone corticosterone (Figure S2A), implying that mice exposed to the CPW paradigm did not experience higher levels of psychological stress than those subjected to a conventional SD paradigm. Moreover, to eliminate the possibility of starvation as a confounding factor, we compared blood glucose levels and glucose tolerance levels between CPW-treated mice and controls. Notably, no significant differences were observed, indicating that the CPW paradigm does not affect metabolic parameters (Figures S2B and S2C). Taken together, these findings strongly indicate that the CPW paradigm deprives mice of sleep without inducing excessive stress or compromising metabolic homeostasis.

Prolonged SD causes a cytokine-storm-like syndrome and mortality

To examine the physiological consequences of extended SD, we subjected adult mice to the CPW paradigm. Within a duration of merely 4 days, ~80% of SD mice experienced premature mortality, dying ranging at 72–96 h following the initiation of SD, which included the subsequent SR period (Figures 1E and S2D). Prior to succumbing, these mice displayed difficulties in maintaining balance and exhibited minimal or no response to gentle touch stimulation. Thorough pathological examination of the SD mice revealed organ damage that affected multiple systems, including the liver (7/8, tissue necrosis with inflammatory cell infiltration) (Figure 1F), spleen (4/8, blurred boundary of pulps) (Figure 1G), lung (3/8, acute lung injury) (Figure 1H), intestine (2/8, structural damage), and kidney (1/8, lesions). Moreover, biochemical analyses conducted on mice that survived 96 h of SD revealed significant elevations in serum alanine aminotransferase (ALT), aspartate aminotransferase (AST), and urea compared with controls (Figures S2E–S2G). Collectively, these findings reveal that prolonged SD causes life-threatening MODS.^{31–33}

To characterize the early-stage phenotypes of SD-induced MODS, we conducted a comprehensive pathological examination

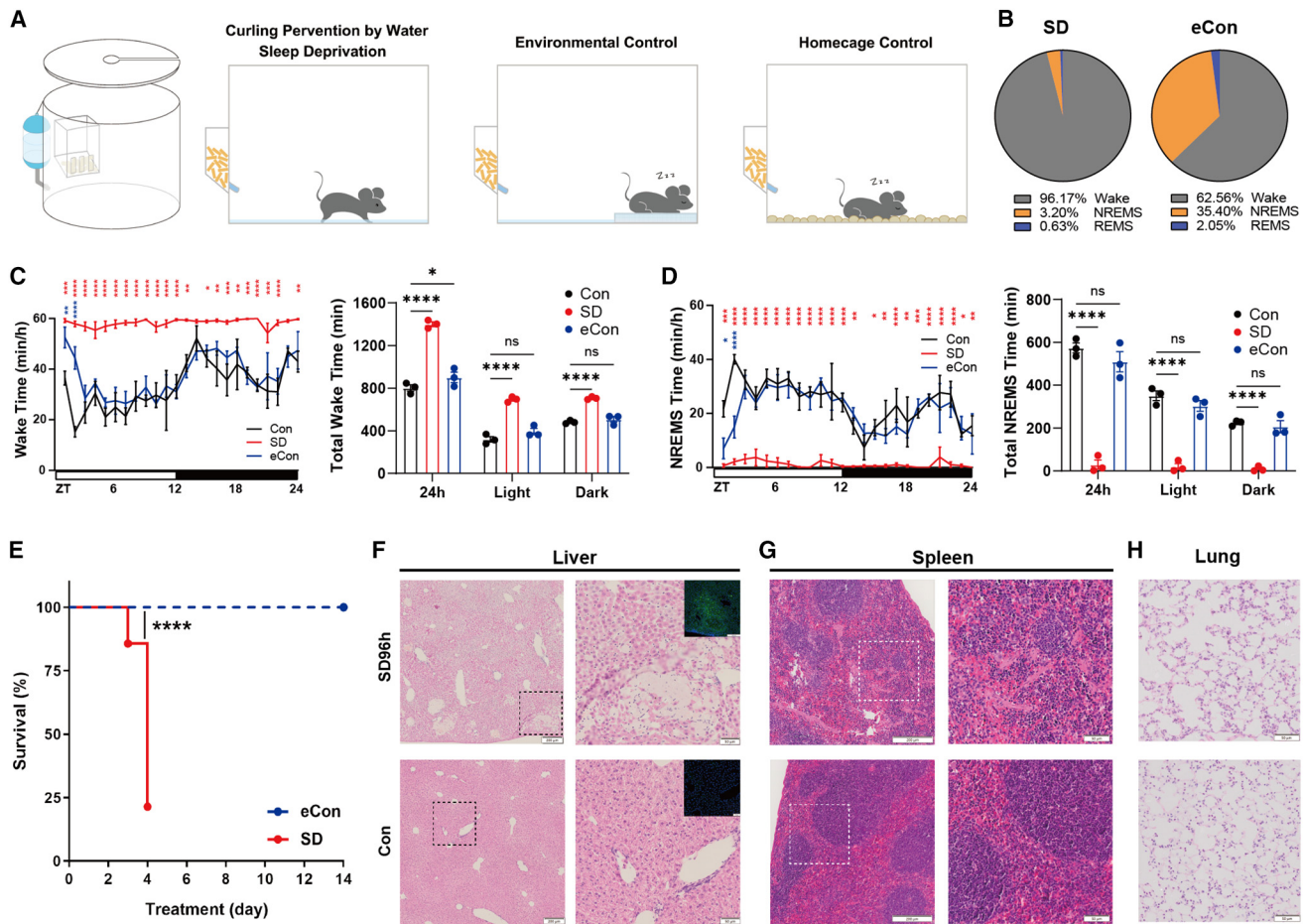


Figure 1. Prolonged sleep deprivation causes systemic inflammation and premature mortality in mice

(A) Schematic showing our prolonged sleep deprivation paradigm. An adult mouse was subjected to one of three conditions, curling prevention by water (CPW), or simply SD, environmental control (eCon), or home-cage control (Con).

(B) The amount of wakefulness, NREMS, and REMS over 24 h for adult mice (n = 3) subjected to SD or eCon.

(C) Hourly plot of wake time (left) and quantification of wake time (right) for adult mice (n = 3) subjected to SD, eCon, or Con.

(D) Hourly plot of NREMS time (left) and quantification of NREMS time (right) for adult mice (n = 3) subjected to SD, eCon, or Con.

(E) Survival curves for C57BL/6J mice subjected to SD (n = 14) or eCon (n = 15).

(F–H) Representative hematoxylin and eosin (H&E) stained sections showing liver with TUNEL fluorescence (blue, DAPI; green, TUNEL) in the inset (F), spleen (G), and lung (H) from SD96h and Con mice.

Data are presented as means \pm SEM. Statistical analysis was performed using two-way ANOVA with Dunnett correction test (C and D) or log-rank test (E). ns, not significant; *p < 0.05; **p < 0.01; ***p < 0.001; ****p < 0.0001.

See also [Figures S1 and S2](#).

of mice subjected to 48 h of SD. Notably, augmented infiltration of neutrophils into the liver was observed in these mice ([Figures S2H and S2I](#)). ROS are known to function as crucial signaling molecules and markers of inflammation.^{34,35} Previous research in flies has implicated that ROS accumulation in gut resulted in sleep loss-induced mortality.⁸ ROS accumulation in intestines has also been observed in mice exposed to SASD for 120 h.⁸ We therefore quantified levels of ROS in the intestines of mice subjected to SD48h and SASD120h. Substantial upregulation of intestinal ROS levels was evident in response to both SD paradigms ([Figure S2J](#)). However, treating these mice with lipoic acid (an antioxidant that neutralizes ROS via electron donation³⁶ and protects against lethality in sleep-loss flies)⁸ or N-acetylcysteine (NAC),

an antioxidant capable of quenching radicals,³⁷ failed to protect against the mortality of mice exposed to the CPW paradigm compared with vehicle controls ([Figures S2K and S2L](#)). Thus, neutralizing ROS alone is insufficient to protect against the initiation of MODS induced by prolonged SD. SD-induced MODS instead resulted from the systemic inflammation association with SD.

In humans, cytokine storms are characterized by an excessive release of proinflammatory cytokines and can cause organ injury, morbidity, and mortality.³⁸ Since SD-subjected mice exhibited organ damage and the infiltration of inflammatory cells, we reasoned that they may have suffered the pathological consequences of cytokine storm.³⁹ To investigate the dynamic

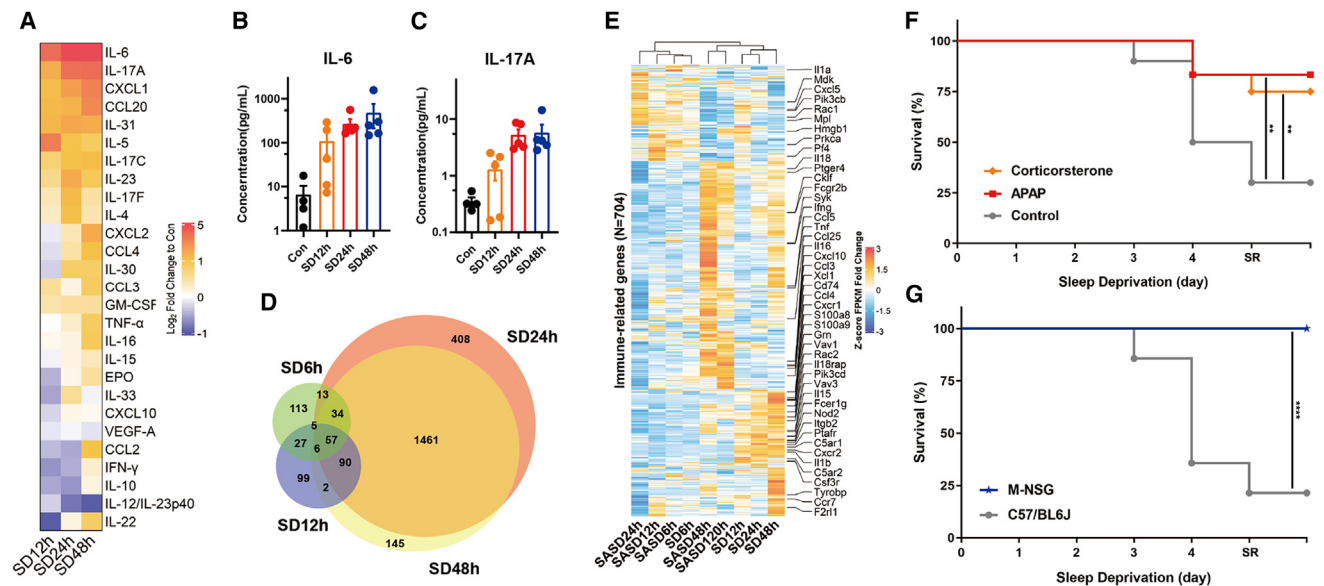


Figure 2. Sleep deprivation induces the accumulation of proinflammatory cytokines in blood

(A) The fold changes of serum cytokines and chemokines in mice (n = 4 or 5) after SD12h, SD24h, and SD48h compared with Con. (B and C) IL-6 (B) and IL-17 (C) serum concentrations in mice (n = 4 or 5) after SD12h, SD24h, and SD48h. (D) Venn diagram showing the overlaps of genes upregulated (FC > 2 over Con) in blood leukocytes from SD6h, SD12h, SD24h, and SD48h mice. (E) RNA-seq heatmap showing the expressions of immune-related genes (including labeled neutrophil relative genes) in blood leukocytes from the mice subjected to SD and SASD at indicated times. (F) Survival curves for mice subjected to SD (SR means 48 h of recovery after SD) with oral administration of corticosterone (n = 12) or acetaminophen (APAP) (n = 12) in the drinking water compared with water controls (n = 10). (G) Survival curves for C57BL/6J (n = 14) or M-NSG (n = 12) mice subjected to SD (SR means 48 h of recovery after SD). Data are presented as means ± SEM. Statistical analysis was performed using log-rank test (F and G). **p < 0.01; ***p < 0.001. See also [Figures S2 and S3](#) and [Table S1](#).

changes in cytokines prior to SD-induced organ damage, serum levels of 27 proinflammatory cytokines and chemokines were measured throughout a SD time course ([Figure 2A](#); [Table S1](#)). The majority of proinflammatory modulators were upregulated as SD progressed. Notably, IL-6 and IL-17A emerged as the most prominent proinflammatory cytokines induced by SD ([Figures 2B and 2C](#)). Both cytokines are known to mediate cytokine storms in humans, and IL-6 is considered an initial driver of this process.³⁹ Additionally, the proinflammatory factors chemokine (C-X-C motif) ligand 1 (CXCL1) and CXCL2 were significantly upregulated after SD ([Figures S3A and S3B](#)). These molecules play roles in neutrophil recruitment⁴⁰ and diapedesis.⁴¹ Further, serum levels of chemokine (C-C motif) ligand 20 (CCL20), which can be upregulated by IL-17A,⁴² also increased following SD ([Figure S3C](#)). To confirm the cytokine-storm-like phenotype during SD, we also conducted time-course measurements of circulating cytokines in SASD-subjected mice. An increase in proinflammatory cytokine levels was observed as early as SASD6h and lasting up to 48 h ([Figure S3D](#); [Table S1](#)). Thus, even partial SD induced increases in proinflammatory cytokines, while continuous and prolonged SD triggered a much more excessive release of cytokines.

To investigate the mechanisms by which SD induces cytokine production, we performed RNA sequencing (RNA-seq) analysis of blood leukocytes throughout an SD time course. Comparative analysis of these transcriptomes revealed that similar sets of

genes were upregulated at SD24h and SD48h, whereas distinct sets of genes were upregulated at SD6h and SD12h ([Figure 2D](#)). Gene ontology (GO) analysis of the genes upregulated at SD24h or SD48h indicated enrichment for genes involved in the positive regulation of immune responses and neutrophil activation ([Figure S3E](#)). However, these enrichments were not observed at SD6h and SD12h. Notably, downregulated genes were enriched for those associated with B cell proliferation and activation ([Figure S3F](#)). Collectively, these findings suggest that the production of cytokines was enhanced as SD progressed, and that different subtypes of leukocytes exhibited distinct responses to SD. Therefore, both serological and transcriptional analyses indicated that SD can regulate systemic levels of proinflammatory modulators and can progressively alter the transcriptional landscape of leukocytes. Together with the MODS phenotypes, these results suggest that SD triggered a cytokine-storm-like syndrome in mice.

To compare the immune responses elicited by different SD paradigms, we also conducted a time-course RNA-seq analysis of blood leukocytes obtained from SASD-subjected mice. A list of immune-related genes (IRGs)⁴³ was used to evaluate immune responses in both SD- and SASD-subjected mice ([Figure 2E](#)). We observed that genes upregulated in the SD24h and SD48h groups were enriched in a previously reported list of genes associated with neutrophils⁴⁴ ([Figure 2E](#)), potentially attributable to dynamic changes in the proportions of different immune-cell

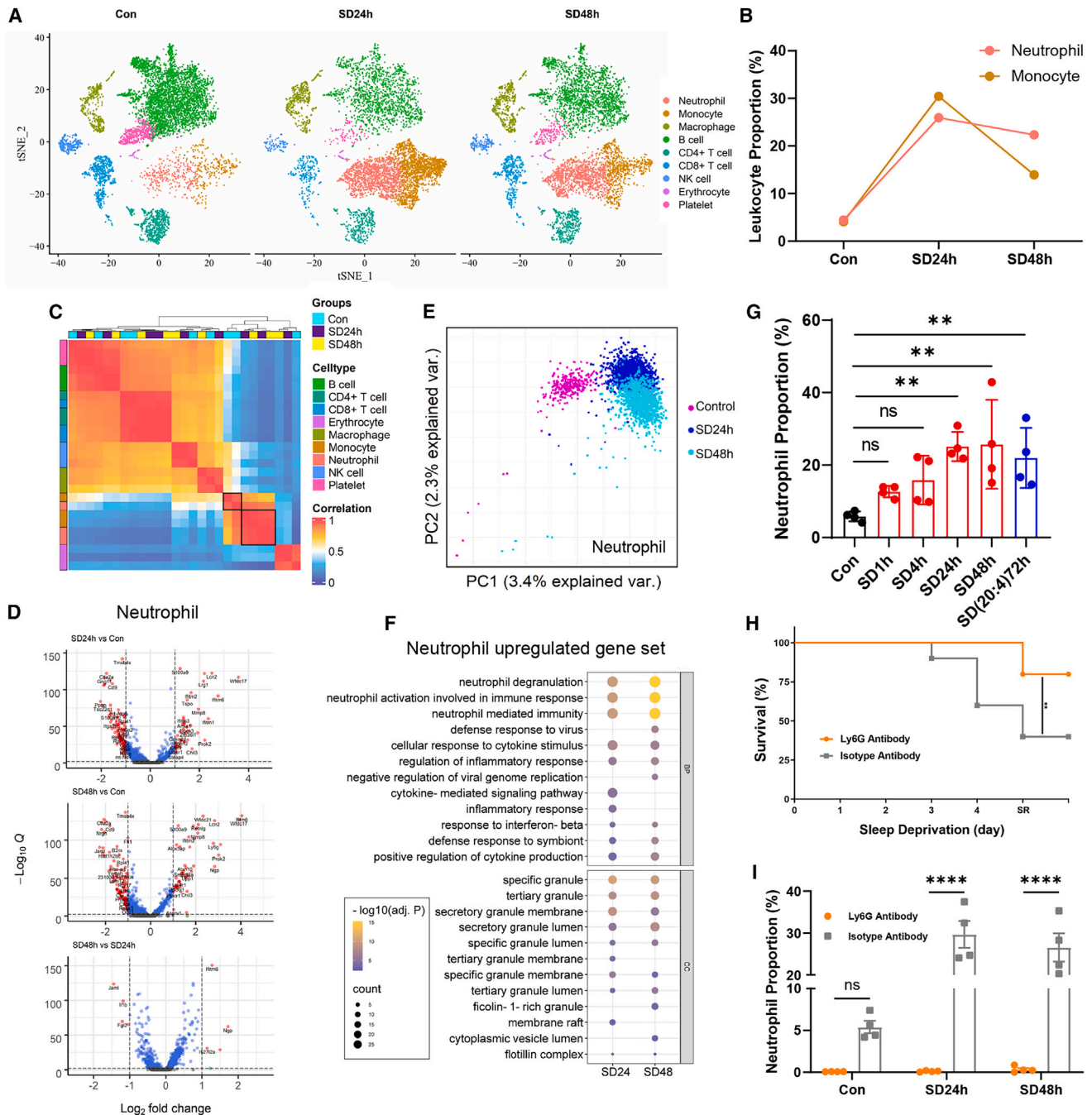


Figure 3. The accumulation of circulating neutrophils contributes to sleep-deprivation-induced mortality

(A) T-distributed stochastic neighbor embedding (t-SNE) plot of scRNA-seq data derived from peripheral blood leukocytes isolated from SD24h, SD48h, and Con mice.

(B) The proportion of neutrophils and monocytes in blood leukocytes in SD24h, SD48h, and Con mice.

(C) Hierarchical clustering using the Pearson correlation coefficient (PCC) of transcriptome alterations for the indicated cell types for SD24h, SD48h, and Con groups. Black boxes highlight neutrophils and monocytes from SD24h and SD48h mice that were separated from Con.

(D) Volcano plots showing differentially expressed genes (DEGs) in comparisons of neutrophils from SD24h, SD48h, and Con mice. Vertical dashed lines denote fold-change thresholds ($|\log_2 FC| = 1$); the horizontal dashed line denotes the q value threshold ($q < 0.01$).

(E) PCA plots showing individual blood neutrophils from SD24h, SD48h, and Con mice.

(F) GO analysis of genes upregulated in neutrophils (SD24h and SD48h) compared with Con. Top 10 ranked GO biological process (BP) and cellular component (CC) terms of individual groups are shown.

(legend continued on next page)

types. Hierarchical clustering and principal-component analysis (PCA) of normalized IRG expression showed that both SD paradigms (SD and SASD) elicited similar patterns of gene expression at 6 h; this pattern persisted up to 24 h in the SASD group. This result was consistent with the increase in serum cytokine levels observed at early stages of both SD and SASD (Figures 2A and S3D). However, as SD progressed, mice subjected to SD or SASD showed distinct patterns of gene expression. SASD48h and SASD120h mice were more similar to controls (Figure S3G), indicating that this conventional paradigm has limitations in preventing sleep, whereas prolonged SD (SD12h, SD24h, and SD48h) resulted in a different pattern of gene expression. These results suggest that leukocyte immune responses depend on the efficiency of SD paradigms, where more efficient SD results in higher levels of neutrophil-related gene expression.

We further investigated the role of cytokines in SD-induced mortality. SD-subjected mice were administered an anti-cytokine-storm agent, such as acetaminophen (APAP)⁴⁵ or corticosterone (the primary glucocorticoid for rodents)⁴⁶ via their drinking water. Mice treated with these agents were resistant to SD-induced mortality (Figure 2F). To extend this analysis, we subjected the immunodeficient NOD.Cg-Prkdc^{scid}Il2rg^{em1Smoc} (M-NSG) mouse line to SD; M-NSG mice lack multiple cytokine signaling pathways (because of a null mutation in the *IL2rg* gene) and exhibit deficiency in mature lymphocytes and natural killer (NK) cells.⁴⁷ Strikingly, all M-NSG mice survived after 96 h of SD (Figure 2G). These M-NSG mice were efficiently deprived of sleep, as confirmed by EEG/EMG-based sleep-wake analysis (Figure S3H), and exhibited NREMS and REMS rebound during the sleep-recovery period (Figure S3I), indicating that sleep homeostasis was unaltered. Further, proinflammatory cytokines were not upregulated in M-NSG mice after SD48h compared with wild-type (WT) mice (Figure S3J; Table S1). Regarding the accumulation of intestinal ROS as a phenotype of systemic inflammation, we observed no obvious accumulation of ROS in the intestines of M-NSG mice after SD (Figure S3K). Consistent with this result, treating WT mice with corticosterone during SD suppressed the accumulation of intestinal ROS compared with controls after SD (Figure S3L). Collectively, these findings suggest that SD-induced mortality can be prevented in mice by suppressing proinflammatory cytokine signaling pathways.

Circulating neutrophils accumulate in response to prolonged SD

Bulk RNA-seq data showed that neutrophil-related genes were upregulated after SD24h (Figure 2E), indicating a potential change in the proportion of leukocyte cell types during SD. To

investigate SD-induced changes in leukocyte subsets, we performed single-cell RNA-seq (scRNA-seq) analyses of leukocytes from control, SD24h, and SD48h mice. Unsupervised clustering revealed 9 cell types based on cluster-specific marker genes (Figure 3A). Among these subsets, the proportions of neutrophils and monocytes were upregulated at SD24h and slightly reduced at SD48h compared with controls, whereas the opposite effect was observed for lymphocytes (Figures 3B and S4A). This increase in neutrophils was consistent with the enrichment of neutrophil-related genes observed in the bulk RNA-seq data (Figure 2E).

To elucidate the effects of SD on distinct cell populations, we performed a cell-type-specific transcriptome correlation analysis. SD caused the most dramatic changes in gene expression in neutrophils and monocytes compared with other cell types, indicating a divergent response to SD among these cell types (Figure 3C). Neutrophils and monocytes exhibited significant transcriptional alterations at SD24h and SD48h compared with controls, whereas minimal changes were observed when comparing SD24h and SD48h (Figure 3D; Table S2). PCA of individual neutrophils revealed clear differences between SD24h, SD48h, and controls (Figure 3E), indicating that neutrophils exhibited distinct transcriptional landscapes in response to SD. In addition, GO analysis of genes upregulated in neutrophils at SD24h and SD48h revealed enrichment for terms including *neutrophil degranulation*, *neutrophil mediated immunity*, and *cytokine-mediated signaling pathway* (Figures 3F, S4B, and S4C). These results suggest that circulating neutrophils accumulated and were activated during SD, which could be mediated by cytokine signaling pathways.

Since the proportion of neutrophils increased in the blood, a phenomenon known as “neutrophilia,” during SD, we explored how SD regulates neutrophil accumulation. Previous studies have shown that acute psychological stress can lead to an increase in circulating neutrophils within an hour, followed by a decline to baseline within 4 h.⁴⁸ Therefore, we used flow cytometry to investigate changes in the proportion of neutrophils in blood leukocytes during SD (Figure S4D). Notably, levels of circulating neutrophils began to steadily increase at 1 h of SD, without a subsequent decline after 4 h, reaching a peak at SD24h and remaining elevated thereafter (Figure 3G). The elevation of circulating neutrophils in mice upon SD was also supported by complete blood count assay results (Table S3). Moreover, the proportion of neutrophils began to decline after 6 h of SR, returning to baseline at 24 h of SR (Figure S4E). The bone marrow is a neutrophil reservoir,⁴⁹ and during SD the proportion of neutrophils decreased in the bone marrow (Figure S4F). These findings collectively suggest that neutrophils are recruited from

(G) The proportion of neutrophils among blood CD45+ leukocytes in mice (n = 4) subjected to SD1h, SD4h, SD24h, SD48h, SD(20:4)72h (i.e., SD at ZT12 for 20 h and resting at ZT8 for 4 h over 72 h), or Con.

(H) Survival curves of mice subjected to SD (SR means 48 h of recovery after SD) with i.p. administration of anti-Ly6G antibody (n = 10) or isotype control antibody (n = 10).

(I) The proportion of neutrophils among blood CD45+ leukocytes in mice (n = 4) treated with anti-Ly6G antibody or isotype control antibody under SD24h, SD48h, or Con.

Data are presented as means ± SEM. Statistical analysis was performed using one-way ANOVA with Dunnett correction test (G), log-rank test (H), or two-way ANOVA with Sidák correction test (I). ns, not significant; **p < 0.01, ****p < 0.0001.

See also Figures S4 and S5 and Tables S2 and S3.

the bone marrow into the bloodstream to sustain elevated levels of circulating neutrophils during SD.

Prolonged total SD is infrequent in humans; however, short sleep duration (<7 h per night) is quite recurrent and is associated with increased risk for health problems and impairs cognitive performance.^{50,51} Therefore, we investigated whether neutrophilia occurs after sleep restriction using the SASD paradigm. We observed a mild yet significant upregulation in circulating neutrophils at SASD48h (Figure S4G), consistent with elevated levels of proinflammatory cytokines (Figure S3D). Many individuals experience extremely short periods of sleep (i.e., sleep only one-third of what is required each day due to heavy workload or social pressure). Further, we used the CPW paradigm to subject mice to a sleep-restriction protocol consisting of 20 h of SD followed by 4 h of SR (SD:SR = 20:4). The proportion of neutrophils increased after 3 and 6 days of sleep restriction (Figures 3G and S4H), indicating that 4 h of sleep per day did not prevent the accumulation of circulating neutrophils in mice experiencing sleep loss. Thus, even restricted daily amounts of sleep can lead to neutrophilia.

To evaluate the contribution of circulating neutrophils to SD-induced mortality, we depleted neutrophils via the intraperitoneal (i.p.) injection of antibodies against Ly6G.⁵² Neutrophil-depleted mice indeed exhibited resistance to SD-induced mortality compared with isotype controls (Figures 3H and 3I), although this resistance to mortality was lower than that seen with M-NSG mice (Figure 2G). We also measured levels of proinflammatory cytokines in neutrophil-depleted mice at SD48h to determine whether neutrophils contributed to cytokine production. These neutrophil-depleted mice still exhibited significant increases in levels of circulating cytokines, particular IL-6 (Figures S4I and S4J; Table S1). These findings suggest that neutrophils primarily function as major cellular effectors in contributing to SD-induced mortality, rather than functioning as a source of cytokines.

Monocytes also exhibited transcriptional alterations during SD (Figures 3C and S5A). Genes upregulated in monocytes after SD were enriched for genes upregulated in IL-6-treated macrophage samples from the GEO database (Figure S5B). Once recruited to tissues, monocytes can differentiate into macrophages. Monocytes and macrophages are members of the mononuclear phagocyte (MoPh) system⁵³ with the latter being an important source of endogenous IL-6.⁵⁴ Thus, we investigated the role of MoPhs in SD-induced mortality by depleting them via i.p. administration of clodronate liposomes.⁵⁵ However, this did not rescue SD-induced mortality (Figure S5C), even though clodronate liposomes efficiently depleted MoPhs in the spleen and liver (organs that were severely damaged by SD), as well as the peripheral blood (Figures S5D–S5H). Therefore, our subsequent analyses focused on circulating neutrophils as a marker of SD-induced systemic inflammation rather than monocytes.

Enhanced efflux of PGD₂ across the BBB during SD triggers inflammation

It is widely acknowledged that sleep is generated by the brain in mammals and that SD impairs brain function, resulting in declines in cognitive performance and memory.⁵⁶ Our finding that SD results in a cytokine-storm-like syndrome motivated us to

assess the role of the brain in triggering this immune response. We initially found that sympathectomy (via i.p. administration of 6-hydroxydopamine hydrobromide [6-OHDA]) did not prevent the accumulation of circulating neutrophils during SD (Figure S6A). We next asked whether transport across the BBB was necessary for SD-induced immune responses. We performed an *in vivo* efflux assay to assess the activity of ABC transporters in BBB endothelial cells using a general ABC transporter substrate, rhodamine B (RHB)^{57,58} (Figure 4A). Previous studies have elegantly demonstrated that BBB efflux is regulated by the endogenous circadian clock and therefore exhibits circadian oscillations.^{57,59} Time-course analysis of BBB efflux in SD-subjected mice revealed significant attenuation of these circadian oscillations and overall enhancement of efflux (Figure 4B). Milder yet significant effects were seen in mice subjected to SASD (Figures S6B and S6C), which is in agreement with their relatively mild immune phenotypes. Furthermore, this increased efflux was also observed using an *ex vivo* ABC transporter efflux assay⁶⁰ (Figure 4C) at two time points: SD6h at ZT6 and SD48h at ZT0 (Figures 4D–4G). These results suggest that the brain affects SD-induced immune responses not via the sympathetic nervous system, but instead through BBB efflux mediated by ABC transporters.

ABC transporters located on the luminal side of capillary epithelial cells mediate active efflux across the BBB. These transporters generally include ABCA2, ABCB1, ABCCs, and ABCG2.⁶¹ We reasoned that if any were involved in SD-induced mortality, pharmacological manipulation of their transport activity would affect the survival curve during SD. Therefore, we administered two ABC antagonists—tariquidar, which targets ABCB1, and MK-571, which targets ABCCs—to mice during SD. Only MK-571 protected against SD-induced mortality (Figures 4H and S6D), suggesting that SD enhances the efflux of ABCC substrates, which subsequently trigger systemic inflammation.

Previous studies have shown that APAP exerts its functions by inhibiting the cyclooxygenase (COX)-1 and COX-2 enzymes, which are known to be involved in PG signaling.⁶² In addition, the anti-inflammatory effects of corticosterone are associated with the inhibition of PG synthesis.⁶³ Given that APAP and corticosterone both protected against SD-induced mortality (Figure 2F), we investigated the role of brain-derived PGs in SD-induced systemic inflammation. PGD₂ is one of the most potent endogenous sleep-promoting substances.^{64,65} Brain-derived PGD₂ is mainly produced by lipocalin-type PG synthase (PTGDS or L-PGDS)⁶⁶; it then enters the cerebrospinal fluid and binds DP1 on the ventral surface of the brain from the basal forebrain to the hypothalamus.⁶⁷ This upregulates extracellular levels of adenosine, which activate sleep neurons in the ventrolateral preoptic area (POA) (VLPO) through adenosine A_{2A} receptors.^{68,69} However, the potential role of PGD₂ in mediating cross-talk between sleep and immunity has not been explored.^{14,70} Thus, we asked whether PGD₂ could trigger SD-induced immune responses. PGD₂ elicits biological responses by activating two G-protein-coupled receptors (GPCRs), DP1 and DP2.⁷¹ Therefore, we simulated an increase in blood PGD₂ levels via the intravenous (i.v.) administration of DP1 and DP2 agonists (treprostinil and L888607, respectively). Only the DP1 agonist increased the

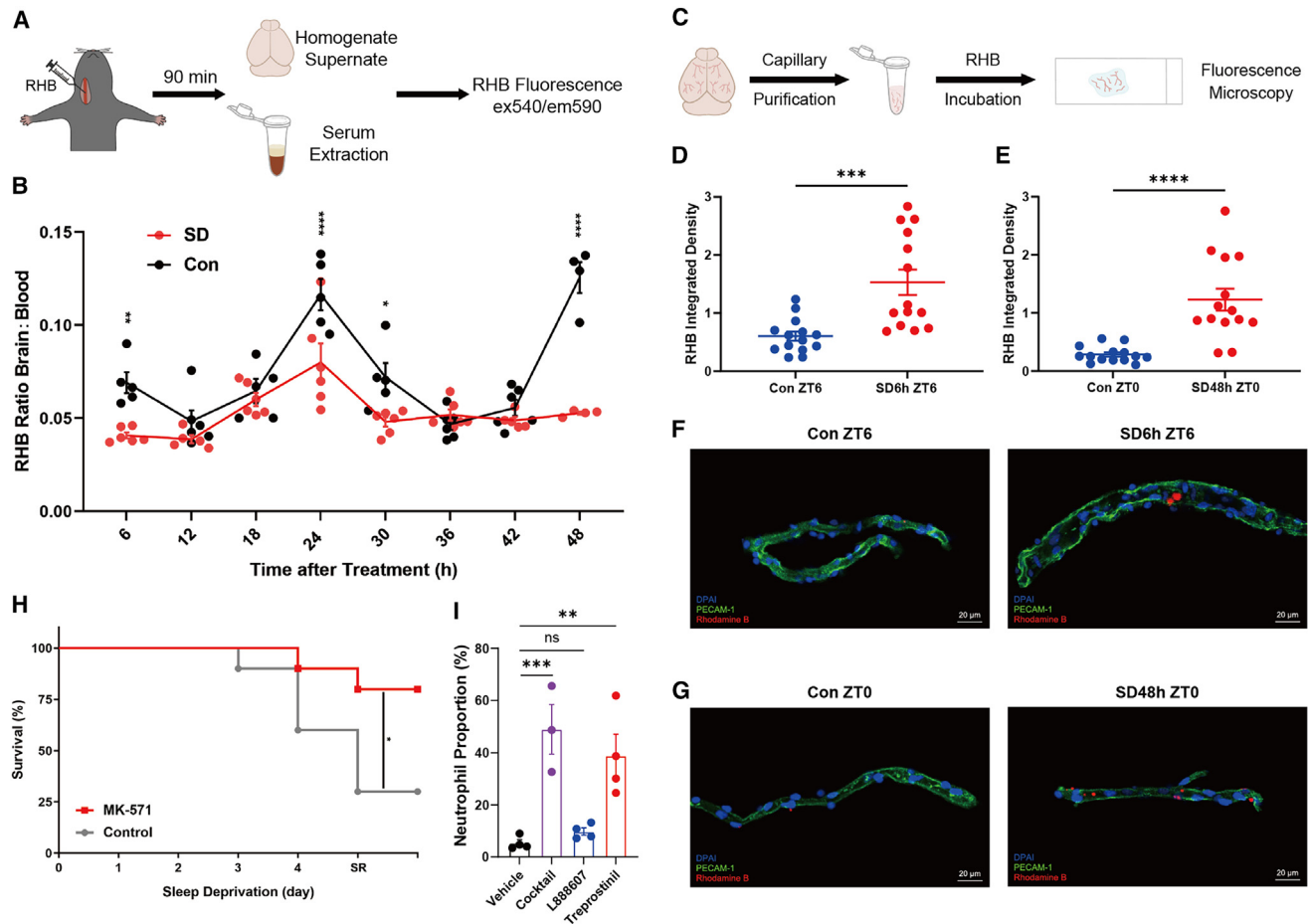


Figure 4. Enhanced efflux through the BBB via ABC transporters induces systemic inflammation during sleep deprivation

(A) Experimental schematic for the *in vivo* BBB ABC transporter efflux assay.

(B) The ratio of rhodamine B (RHB) levels in brain homogenate vs. serum in mice ($n = 4-6$) after the indicated times under SD or Con; a lower ratio indicates enhanced BBB ABC-transporter-mediated efflux.

(C) Experimental schematic for the *ex vivo* BBB ABC transporter efflux assay.

(D and E) RHB fluorescence integrated density in brain capillaries ($n = 14$) of SD6h (D) or SD48h (E) mice and ZT6 or ZT0 controls.

(F and G) Representative confocal microscopy images showing fluorescence of RHB (red), PECAM-1 (green), and DAPI (blue) in brain capillaries of SD6h (F) or SD48h (G) mice and corresponding controls.

(H) Survival curves for mice subjected to SD (SR means 48 h of recovery after SD) with oral administration of MK-571 ($n = 10$) in the drinking water compared with water controls ($n = 10$).

(I) The proportion of neutrophils among blood CD45+ leukocytes in mice ($n = 3$ or 4) 16 h after *i.v.* administration of treprostinil (DP1 agonist), L888607 (DP2 agonist), cocktail (treprostinil + L888607), or vehicle control.

Data are presented as means \pm SEM. Statistical analyses were performed using two-way ANOVA with Šidák correction test (B), two-tailed unpaired t test (D and E), log-rank test (H), or one-way ANOVA with Dunnett correction test (I). ns, not significant; * $p < 0.05$; ** $p < 0.01$; *** $p < 0.001$; **** $p < 0.0001$.

See also Figure S6.

proportion of neutrophils among blood leukocytes in a dose-dependent manner in resting mice (Figures 4I and S6E). Importantly, this DP1 agonist also increased levels of serum IL-6 (Figure S6F). These findings suggest that PGD₂ plays a role in brain-mediated immune responses during SD.

GPCR-activation-based (GRAB) sensors are potent tools for detecting neurochemical molecules, enabling one to monitor bioactive compounds with high sensitivity and specificity.⁷²⁻⁷⁴ To measure PGD₂ levels in the brain during SD, we sought to develop a GRAB sensor following the previously reported workflow.^{75,76} We inserted a conformation sensitive circularly permu-

tated enhanced GFP (cpEGFP) module into the DP1 (Figure 5A). By introducing and screening mutations in the linkers between cpEGFP and DP1, we successfully developed the GRAB_{PGD₂-1.0} sensor (Figures 5B and S6G). This fluorescent sensor exhibited specific responses to PGD₂ with a maximum $\Delta F/F_0$ of $\sim 200\%$ under 10 μM (Figure 5C). The apparent affinity for PGD₂ was ~ 10 nM, which is close to the binding affinity of WT DP1.⁷⁷ We also measured dose-dependent binding of the sensor to other brain PGs, namely PGE₂, PGF_{2a}, and PGI₂. Maximum responses and apparent affinity were both lower compared with PGD₂ (Figure 5C). We therefore used GRAB_{PGD₂-1.0}-expressing HEK cells to assess

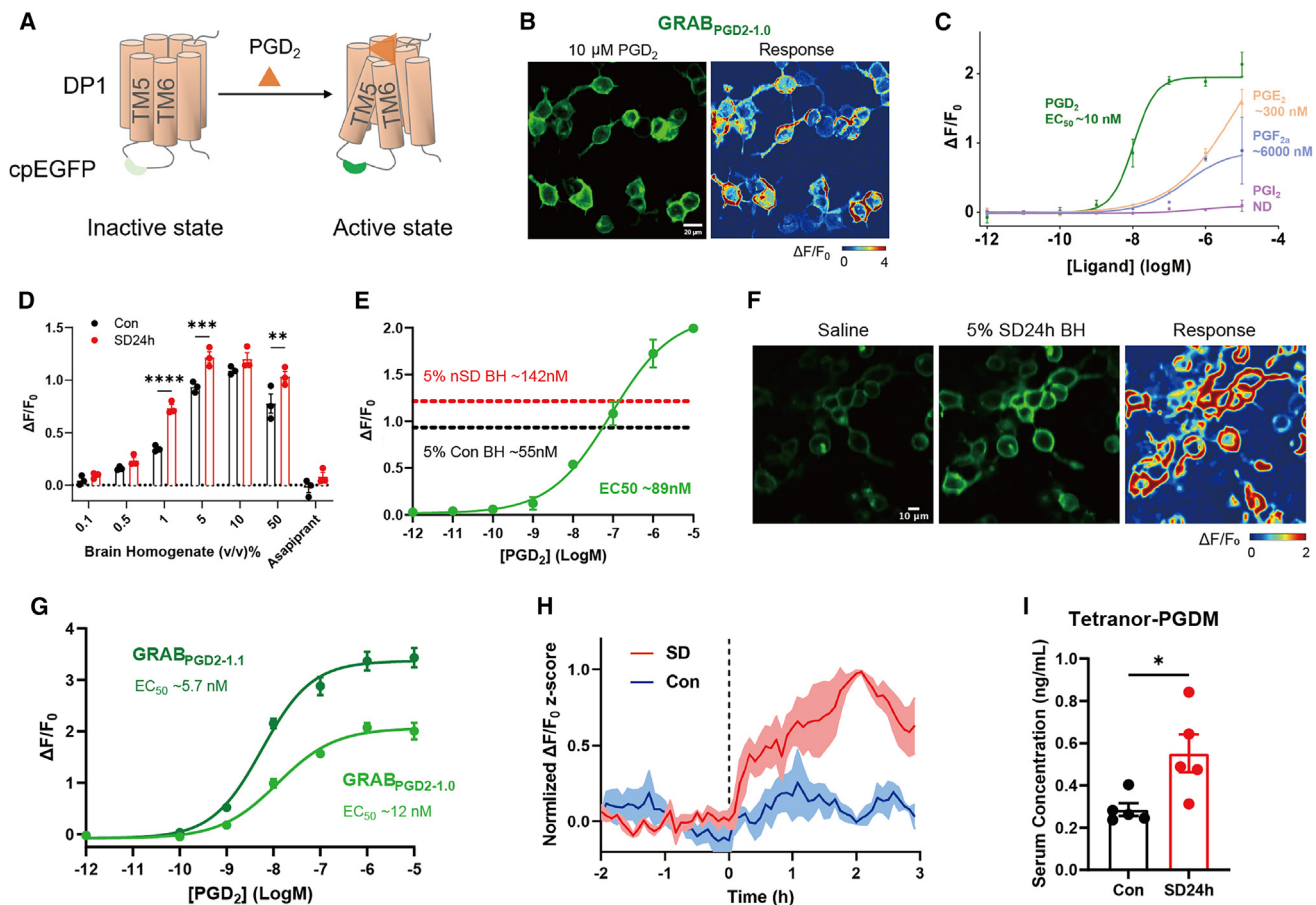


Figure 5. The genetically encoded PGD_2 sensor ($GRAB_{PGD_2}$) reveals increased levels of PGD_2 in the brain during sleep deprivation

(A) Schematic diagram illustrating the principle of the $GRAB_{PGD_2}$ sensor.

(B) Representative fluorescence image and fluorescence response to $10\ \mu M$ PGD_2 in HEK293T cells expressing $GRAB_{PGD_2-1.0}$.

(C) Dose-response curves measured in HEK293T cells expressing $GRAB_{PGD_2-1.0}$ for PGD_2 , PGE_2 , $PGF_{2\alpha}$, and PGI_2 ($n = 3$ wells) with the corresponding EC_{50} value.

(D) Fluorescence response measured in HEK293T cells expressing $GRAB_{PGD_2-1.0}$ with the indicated concentrations (v/v) of brain homogenate (BH) sampled from SD24h and Con mice ($n = 3$ wells), followed by $1\ \mu M$ asapirant.

(E) Dose-response curve measured in HEK293T cells expressing $GRAB_{PGD_2-1.0}$ ($n = 3$ wells). The dashed red line represents the fluorescence change of 5% SD24h BH; the dashed black line represents the fluorescence change of 5% Con BH.

(F) Representative fluorescence images showing expression and fluorescence response to 5% SD24h BH in HEK293T cells expressing $GRAB_{PGD_2-1.0}$.

(G) Dose-response curves measured in HEK293T cells ($n = 3$ wells) expressing $GRAB_{PGD_2-1.0}$ or $GRAB_{PGD_2-1.1}$ for PGD_2 with the corresponding EC_{50} values and maximum responses.

(H) Time course of normalized z score of fluorescence responses of $GRAB_{PGD_2-1.1}$ in the POA of freely moving mice ($n = 3$) before and after the indicated procedure (started at 0 h).

(I) Serum tetranor-PGDM concentrations in mice ($n = 5$) subjected to SD24h or Con.

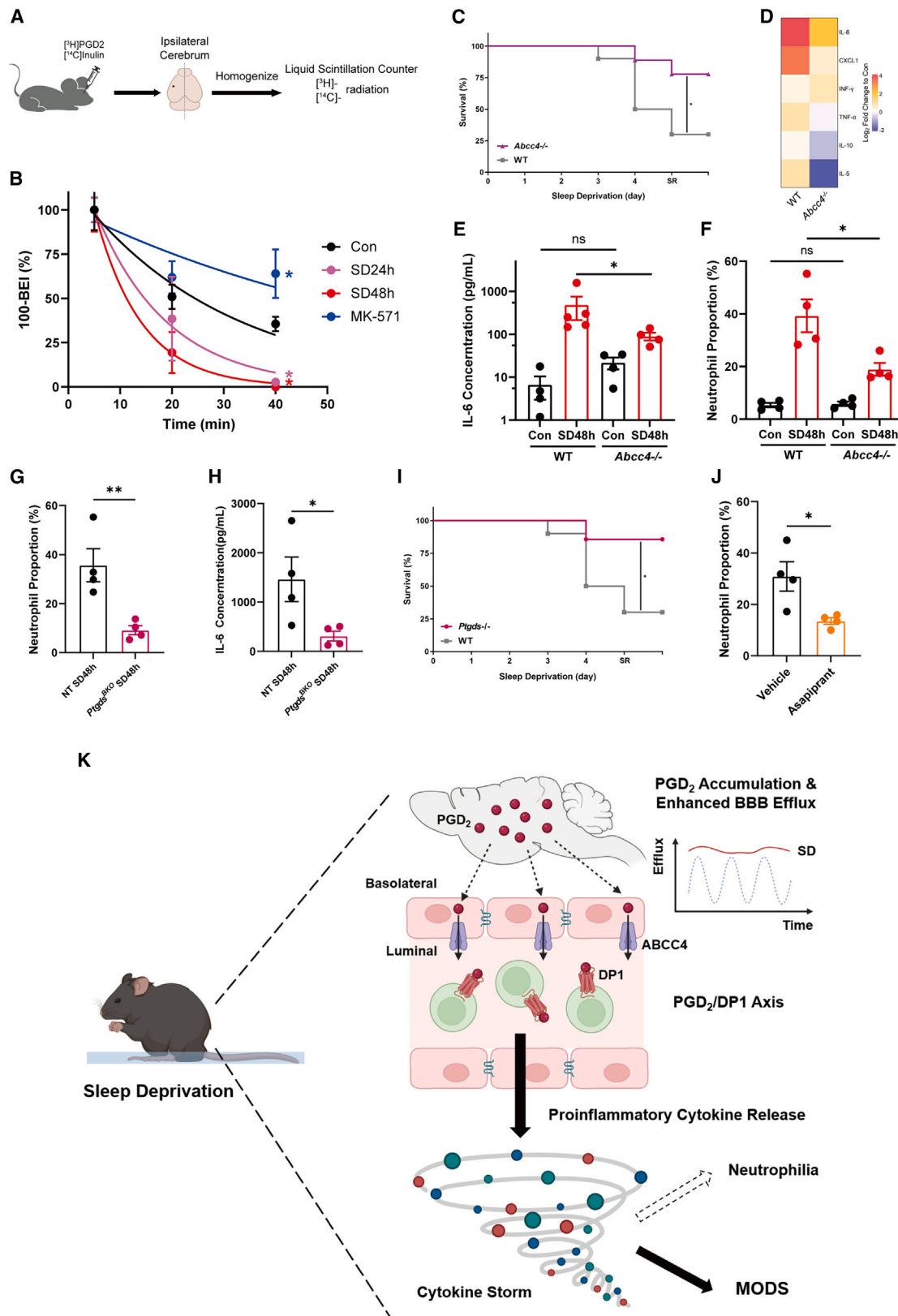
Data are presented as means \pm SEM. Statistical analysis was performed using two-way ANOVA with Šidák correction test (D) or two-tailed unpaired t test (I). * $p < 0.05$; ** $p < 0.01$; *** $p < 0.001$; **** $p < 0.0001$.

See also Figure S6.

levels of brain PGD_2 . Brain homogenates (BHs) were generated from SD24h and control mice and applied to $GRAB_{PGD_2-1.0}$ -expressing HEK cells. We observed a 158% increase in brain PGD_2 in SD24h mice compared with controls (Figures 5D–5F), indicating that SD elevates levels of PGD_2 in the brain.

As our ultimate goal was to utilize the PGD_2 sensor in the brain, we next evaluated the performance of $GRAB_{PGD_2-1.0}$ in cultured rat primary cortical neurons. We assessed dose-dependent responses and the molecular specificity of $GRAB_{PGD_2-1.0}$ -ex-

pressing neurons. The maximum $\Delta F/F_0$ in response to $10\ \mu M$ PGD_2 exceeded 350%, and the DP1 antagonist, asapirant, rapidly attenuated this fluorescence response (Figure S6H). Although the half maximal effective concentration (EC_{50}) of $GRAB_{PGD_2-1.0}$ in cultured neurons was $\sim 165\ nM$ (Figures S6I and S6J), which was much higher than measured in HEK cells, $GRAB_{PGD_2-1.0}$ still exhibited specific responses to PGD_2 in cultured neurons, while responding only slightly to structurally similar signaling lipids (Figure S6K). Finally, we used $GRAB_{PGD_2-1.0}$ -expressing



(legend on next page)

neurons to measure PGD₂ levels in BHs from SD mice. This revealed an increase in PGD₂ levels after SD (Figures S6L and S6M), although not as dramatic as that seen with HEK cells. These results suggest that although GRAB_{PGD2-1.0} can specifically and sensitively detect PGD₂ *in vitro*, it may not be suitable for monitoring changes in brain PGD₂ levels *in vivo*.

Thus, to develop an advanced PGD₂ sensor with enhanced apparent affinity and response, we introduced and screened more than 600 mutants to optimize the GRAB_{PGD2-1.0} linker (Figure S6N). The optimized PGD₂ sensor, namely GRAB_{PGD2-1.1}, exhibited specific responses to PGD₂ with a maximum $\Delta F/F_0 \sim 340\%$ and ~ 5.7 nM affinity in HEK cells, representing an improvement of $\sim 170\%$ and $\sim 110\%$, respectively, compared with GRAB_{PGD2-1.0} (Figure 5G). We then used this improved PGD₂ sensor to perform *in vivo* recordings. As PGD₂ promotes sleep and *Ptgds*-expressing neurons are located in the POA,^{78,79} we stereotactically injected recombinant adeno-associated viruses (AAVs) expressing GRAB_{PGD2-1.1} into the POA and then used an optical fiber to monitor extracellular PGD₂ levels in freely moving mice (Figures S6O and S6P). Levels of fluorescence increased in the POA in response to SD. Levels peaked at 2 h of SD and gradually decreased, which could be attributed to the enhanced BBB efflux after SD (Figure 4A), but still higher compared with the controls thereafter (Figure 5H). Since PGD₂ is rapidly metabolized in the circulation with a half-life ~ 90 sec,⁸⁰ to assess levels of PGD₂ in the blood, we measured levels of a more stable ultimate PGD₂ metabolite, tetranor Prostaglandin D Metabolite (tetranor-PGDM).^{81,82} Elevated levels of tetranor-PGDM in the blood after SD (Figure 5I) indicated that hyperproduced brain PGD₂ was transported through BBB and accumulated in the blood. Our GRAB_{PGD2} sensor effectively demonstrated that SD results in a dramatic increase in PGD₂ levels in the brain.

Reportedly, the efflux transporter ABCC4 mediates the conveyance of PGs, including PGD₂,^{83,84} across the BBB. To investigate whether PGD₂ efflux increases with SD, we employed the brain efflux index (BEI) assay^{84,85} using [³H]-labeled PGD₂ ([¹⁴C]-inulin was used as an internal control; Figure 6A). The BEI (in which 100-BEI [%] represents the retained ratio of [³H]-PGD₂ in the brain) was measured over time. Analyzing

SD24h, SD48h, and control mice revealed a substantial increase in PGD₂ efflux across the BBB during SD (Figure 6B). Notably, administration of MK-571 suppressed this PGD₂ efflux. Collectively, these findings indicate that brain-derived PGD₂ accumulates in blood with enhanced efflux and then plays an essential role in SD-induced systemic inflammation.

Finally, we investigated whether blocking the PGD₂/DP1 axis could alleviate the systemic inflammation observed during SD. The efflux of brain-derived PGD₂ is blocked in *Abcc4*^{-/-} mice, resulting in protection against SD-induced mortality (Figure 6C). Levels of circulating proinflammatory cytokine, particular IL-6, and circulating neutrophils were also attenuated in *Abcc4*^{-/-} mice subjected to SD48 compared with WT controls (Figures 6D–6F; Table S1). To attenuate the synthesis of brain-derived PGD₂, we used the AAV-based adult brain chimeric-knockout (KO) platform^{86,87} to deplete PTGDS, namely *Ptgds*^{BKO} (Figure S6Q). *Ptgds*^{BKO} mice subjected to SD48h showed attenuated induction of circulating neutrophils and serum IL-6 compared with nontargeted (NT) control mice (Figures 6G and 6H). Further, the genetic *Ptgds*^{-/-} (conventional KO) mice were resistant to SD-induced mortality (Figure 6I). Oral administration of the DP1 antagonist, asapirant, inhibited DP1-mediated signaling and significantly reduced the proportion of neutrophils among blood leukocytes in SD24h mice (Figure 6J). Moreover, to exclude the possibility that inhibition of brain-derived PGD₂/DP1 axis confers some general protection against sepsis, we examined whether modulating the PGD₂/DP1 axis affects mortality in a classic cecal ligation and puncture (CLP) mouse model.^{88,89} Briefly, the survival curves revealed that the supply of asapirant or MK-571 did not affect CLP-induced sepsis (Figures S6R and S6S); nor was mortality affected in *Abcc4*^{-/-} mice (Figure S6T). Taken together, these results reveal a potent pathway by which sleep regulates the immune system. SD enhances PGD₂ efflux across the BBB, which then triggers systemic inflammation (Figure 6K).

DISCUSSION

Here we introduce the CPW paradigm, which more efficiently induces SD. We then used this paradigm to elucidate the

Figure 6. Sleep deprivation triggers enhanced efflux of PGD₂ from the brain, which induces a life-threatening cytokine storm as sleep deprivation is prolonged

- (A) Experimental schematic for the PGD₂ brain efflux index (BEI) assay.
 (B) Time course of [³H]-PGD₂ remaining percentage (100-BEI) in the ipsilateral cerebrum after microinjection in SD24h, SD48h, Con, or MK-571-treated mice (n = 2 or 3 per group); lines indicate the semi-log nonlinear regressions of individual groups.
 (C) Survival curves of *Abcc4*^{-/-} (n = 9) or WT mice (n = 10) subjected to SD (SR means 48 h of recovery after SD).
 (D) Serum cytokines and chemokines in *Abcc4*^{-/-} and WT mice (n = 4) after SD48h.
 (E) IL-6 serum concentrations in *Abcc4*^{-/-} and WT mice (n = 4) for SD48h and Con groups.
 (F) The proportion of neutrophils among blood CD45+ leukocytes in *Abcc4*^{-/-} and WT mice (n = 4) for SD48h and Con groups.
 (G and H) The proportion of neutrophils among blood CD45+ leukocytes (G) and IL-6 serum concentrations (H) for SD48h mice injected with AAV-sgRNA^{PTGDS} (*Ptgds*^{BKO}) (n = 4) or AAV-sgRNA^{NT} (NT) (n = 4).
 (I) Survival curves of *Ptgds*^{-/-} (n = 7) or WT mice (n = 10) subjected to SD (SR means 48 h of recovery after SD).
 (J) The proportion of neutrophils among blood CD45+ leukocytes in SD24h mice with oral administration of asapirant (a DP1 antagonist, n = 4) or vehicle (n = 4).
 (K) Schematic model of brain-immunity interactions and consequences during sleep deprivation. Sleep deprivation both disrupts the circadian oscillation of ABC transporter efflux across the BBB and enhances general PGD₂ efflux from the brain. PGD₂ induces the accumulation of proinflammatory cytokines in the periphery and the accumulation of circulating neutrophils, which results in increased immune-cell infiltration into organs. As sleep deprivation is prolonged, the lasting sleep deprivation-induced proinflammatory cytokines cause life-threatening multiple organ dysfunction syndrome.
 Data are presented as means \pm SEM. Statistical analysis was performed using two-way ANOVA with Holm-Sidak correction test (B), log-rank test (C and I), two-tailed unpaired U test (E and F), or unpaired two-tailed t test (G, H, and J). ns, not significant; *p < 0.05; **p < 0.01.
 See also Figure S6 and Table S1.

mechanism by which prolonged SD triggers a life-threatening cytokine-storm-like syndrome in mice. SD induced an accumulation of PGD₂ in the brain, and subsequent ABCC4 transporter-mediated efflux of brain-derived PGD₂ across the BBB resulted in the excessive production of proinflammatory cytokines, ultimately leading to a cytokine-storm-like phenotype and MODS. Further, we demonstrated that the enhanced efflux of brain-derived PGD₂ drove the immune consequences caused by chronic SD, including neutrophilia and the induction of proinflammatory cytokines.

The CPW paradigm is extremely effective in depriving mice of sleep, forcing the animals to remain awake 96% of the time. The CPW paradigm is thus more effective than the conventional SASD or moving treadmill paradigms,⁹⁰ and comparable with the DOW paradigm for rats^{11,12} without the need for real-time EEG/EMG monitoring. In addition, because the gentle-handing paradigm is labor intensive,²⁴ the CPW paradigm is more suitable for long-term SD or high-throughput experiments, as it requires very little human supervision. Since the water-filled environment in the CPW paradigm results in upregulation of serum corticosterone levels (comparable with those seen with the SASD paradigm) (Figure S2A), indicating that the CPW environment is still stressful. Thus, the CPW paradigm may not be suitable for elucidating the contribution of sleep pressure in the stress responses during SD. We also cannot fully rule out a role for stress in the downstream physiological and immune consequences of SD. Therefore, further investigations into the relationship between stress and the adverse effects of SD are still needed.

EEG/EMG electrophysiology monitoring is widely accepted as the gold standard for sleep/wake analysis as it can be used to accurately distinguish between different sleep stages. However, the noticeable increase in EMG signals in SD mice indicates increased muscular excitation (Figure S1A), which could be attributed to the frequent muscular tension experienced during wakefulness. Increased muscular excitation is a common characteristic of SD and prolonged wakefulness and may contribute to a certain extent of the immune consequences of long-term SD, as muscular injury can induce inflammation.^{91,92}

The accumulation of ROS in the intestines is an immune consequence of SD. The ROS accumulation in gut is considered the cause of death in SD flies.⁸ In our study, inhibition of immune function or inflammation (via genetic manipulation or pharmacological intervention) protected against both SD-induced mortality and intestinal ROS accumulation in SD mice (Figures S3K and S3L). Since ROS are key signaling molecules and markers of inflammation,^{34,35} intestinal ROS accumulation is thus considered an immune consequence of SD in mice.

Chronic SD is associated with a wide range of adverse health effects, including cognitive deficits, hypertension, neurological diseases, anxiety, depression, and inflammation.^{23,56} Further, it is known that PGD₂ signaling regulates many of the physiological consequences of SD.⁹³ PGD₂ mediates Amyloid beta (Aβ)-induced neuronal damage,⁹⁴ and intracerebroventricular (i.c.v.) administration of PGD₂ exhibits anxiolytic-like behavior via the DP1 receptor in mice.⁹⁵ PGD₂ functions as a potent sleep-promoting molecule: both KO of *Ptgds* and inhibition of PTGDS with SeCl₄ have been shown to reduce sleep rebound after SD

in mice,^{65,96} findings suggesting that altered sleep rebound may contribute to the reduced SD-induced mortality we observed in the *Ptgds*^{-/-} mice. It is widely accepted that the PGD₂/DP1 axis regulates sleep^{64,67} in the brain, and the PGD₂/DP2 axis is thought to regulate multiple immune responses.^{97,98} Taken together, the PGD₂/DP1 axis remains an important candidate for mediating the adverse effects of SD.

Our CPW paradigm deprives mice of sleep for extended periods of time (>96 h) with high efficiency (depriving mice of 96% of their sleep) providing a unique opportunity to investigate the physiological consequences of long-term SD. For example, following SR after SD24h, the proportion of neutrophils in the blood gradually returned to baseline (Figure S4E), indicating that SD-induced immune phenotypes are reversible. However, further SD resulted in sustained high levels of circulating neutrophils and mortality. This raises an interesting question: what physiological consequences of SD are reversible? SD-induced physiological changes arise from two potential sources, the CNS and the peripheral system. In the CNS, long-term wakefulness leads to consistent firing of wake-activated neurons, resulting in neuronal morphometric changes and neuron loss in some vulnerable brain regions.^{99,100} In the peripheral systems, multiple systems experience oxidation stress accumulation or metabolic disorder during prolonged wakefulness, causing cellular-level damage in these systems and organs.^{21,101,102} This stress may initially be low and reversible, whereas chronic accumulation or dysregulation of stress homeostasis can trigger disease, which is irreversible. Moreover, in a human study of chronic sleep restriction, individuals experience physiological and psychological impairment, but many healthy adults did not subjectively perceive stress after SR.¹⁰³ This indicates a dissociation between subjective and objective stress responses, which may be attributed to the fact that irreversible stress responses at the cellular level are reversible or even undetectable at the organismal level. However, the turning point at which the cumulative effects of SD lead to irreversible consequences, and whether preventing PGD₂ efflux during SD can extend this turning point, require further investigation.⁹⁰

Since sleep is deeply involved in a wide range of biological processes, including immune regulation,⁴ cognition performance,⁵ and metabolism,⁶ insufficient sleep has adverse effects on health. Our study introduced a SD paradigm and revealed the involvement of brain-derived PGD₂ in immune dysregulations during SD. These findings lay the foundation for deciphering mechanisms by which SD drives other adverse health effects and how sleep interacts with other biological processes.

Limitations of the study

Given that clodronate liposomes do not completely deplete MoPhs, our approach was unable to unambiguously delineate the impacts of MoPhs on the observed SD-induced immune phenotypes. A previous study reported that clodronate liposomes can be ingested by both MoPhs and polymorphonuclear neutrophils (PMNs),¹⁰⁴ so a genetic model that depletes MoPhs to a fuller extent would be welcomed to support investigations into the roles of MoPhs in SD-induced immune phenotypes.

It also bears mention that we have not identified the immune cells that initiate the observed excessive production of proinflammatory cytokines in response to brain-derived PGD₂. *Ptgdr* KO mice (ideally including both *Ptgdr*^{-/-} and various cell type-specific *Ptgdr* KOs) would be useful for further elucidating how brain-derived PGD₂ works through DP1 to regulate the immune system.

STAR★METHODS

Detailed methods are provided in the online version of this paper and include the following:

- **KEY RESOURCES TABLE**
- **RESOURCE AVAILABILITY**
 - Lead contact
 - Materials availability
 - Data and code availability
- **EXPERIMENTAL MODEL AND STUDY PARTICIPANT DETAILS**
 - Mice
 - Cell lines
- **METHOD DETAILS**
 - Curling Prevention by Water (CPW) paradigm
 - Stand Alone Sleep Deprivation (SASD) paradigm
 - EEG/EMG-based sleep/wake analysis
 - Necropsy and histopathology of dead mice
 - H&E staining
 - TUNEL assay
 - Immunofluorescence staining
 - Administration of drugs during CPW procedure
 - Blood glucose detection
 - Blood leukocyte separation
 - Leukocyte bulk RNA sequencing
 - Leukocyte single-cell RNA sequencing
 - Detection of ROS in mouse small intestine
 - *In vivo* neutrophil depletion
 - Neutrophil proportion detection
 - *In vivo* mononuclear phagocyte depletion
 - Serum extraction
 - Serum cytokine & chemokine screen assay
 - ELISA
 - Chemical sympathectomy
 - *In vivo* BBB efflux assay with rhodamine B
 - Mouse brain vessel purification
 - *Ex vivo* ABC transport assay with rhodamine B
 - PGD₂ Brain Efflux Index (BEI) Assay
 - GRAB_{PGD2} Development
 - Fluorescence imaging of HEK293T cells expressing GRAB_{PGD2}
 - Confocal imaging of cultured neurons expressing GRAB_{PGD2-1.0}
 - Fiber photometry recording and analysis of GRAB_{PGD2-1.1}
 - Tetranor-PGDM concentration measurement
 - Adult brain chimeric-KO rAAV construction
 - Retro-orbital rAAV injection
 - Brain lysate preparation and immunoblotting

- DP1 and DP2 agonist administration
- Cecal ligation and puncture (CLP) model
- **QUANTIFICATION AND STATISTICAL ANALYSIS**

SUPPLEMENTAL INFORMATION

Supplemental information can be found online at <https://doi.org/10.1016/j.cell.2023.10.025>.

ACKNOWLEDGMENTS

We thank Drs. Garret FitzGerald of U Penn, John Hogenesch of CCHMC, Andrew Liu of U Florida, Yelin Chen of IRCBC, Tongfei Wang of CIBR, Weiliang Fan of Sironax, Mo Xu and Meng-Qiu Dong of NIBS, and members of the Neuroscience Pioneer Club for stimulating discussions; Shitang Huang of PKU for technical assistance on radioisotope handling; and Jianhua Sui of NIBS on antibody-mediated depletions of neutrophils and monocytes. Figures 6K and S6O were created with [BioRender.com](https://www.biorender.com). This research was supported by funds from the Ministry of Science and Technology of the People's Republic of China STI2030-Major Projects (2021ZD0203400), the National Natural Science Foundation of China (31971090), the Beijing Municipal Government, and Tsinghua University.

AUTHOR CONTRIBUTIONS

D.S. and E.E.Z. conceived of the study. D.S. and K.L. executed most of the experiments with guidance from E.E.Z. Y.Y. and B.L. developed GRAB_{PGD2} and performed the *in vitro* PGD₂ detection assay under supervision of Y.L. G.R. performed hematoxylin and eosin (H&E) and immunofluorescence staining, with assistance from C.C. L.L. performed EEG/EMG recordings and analyses to assess SD efficiency under the supervision of M.L. Q. Li performed the sleep-rebound assay and adult brain chimeric-KO platform under supervision of Q. Liu. Y.M. performed tetranor-PGDM measurements with liquid chromatography-mass spectrometry (LC-MS). S.-Q.L. provided intellectual input. X.-Y.C. and Z.L. helped with the BEI assay. D.S., K.L., and E.E.Z. wrote the manuscript, which all authors commented on.

DECLARATION OF INTERESTS

The authors declare no competing interests.

Received: March 5, 2023

Revised: August 17, 2023

Accepted: October 25, 2023

Published: November 27, 2023

REFERENCES

1. Campbell, S.S., and Tobler, I. (1984). Animal sleep: a review of sleep duration across phylogeny. *Neurosci. Biobehav. Rev.* 8, 269–300.
2. Anafi, R.C., Kayser, M.S., and Raizen, D.M. (2019). Exploring phylogeny to find the function of sleep. *Nat. Rev. Neurosci.* 20, 109–116. <https://doi.org/10.1038/s41583-018-0098-9>.
3. Krueger, J.M., Frank, M.G., Wisor, J.P., and Roy, S. (2016). Sleep function: toward elucidating an enigma. *Sleep Med. Rev.* 28, 46–54. <https://doi.org/10.1016/j.smrv.2015.08.005>.
4. Schiller, M., Ben-Shaanan, T.L., and Rolls, A. (2021). Neuronal regulation of immunity: why, how and where? *Nat. Rev. Immunol.* 21, 20–36. <https://doi.org/10.1038/s41577-020-0387-1>.
5. Walker, M.P. (2009). The role of sleep in cognition and emotion. *Ann. N. Y. Acad. Sci.* 1156, 168–197. <https://doi.org/10.1111/j.1749-6632.2009.04416.x>.
6. Benington, J.H., and Heller, H.C. (1995). Restoration of brain energy metabolism as the function of sleep. *Prog. Neurobiol.* 45, 347–360. [https://doi.org/10.1016/0301-0082\(94\)00057-o](https://doi.org/10.1016/0301-0082(94)00057-o).

7. Shaw, P.J., Tononi, G., Greenspan, R.J., and Robinson, D.F. (2002). Stress response genes protect against lethal effects of sleep deprivation in *Drosophila*. *Nature* *417*, 287–291. <https://doi.org/10.1038/417287a>.
8. Vaccaro, A., Kaplan Dor, Y., Nambara, K., Pollina, E.A., Lin, C., Greenberg, M.E., and Rogulja, D. (2020). Sleep loss can cause death through accumulation of reactive oxygen species in the gut. *Cell* *181*, 1307–1328.e15. <https://doi.org/10.1016/j.cell.2020.04.049>.
9. Stephenson, R., Chu, K.M., and Lee, J. (2007). Prolonged deprivation of sleep-like rest raises metabolic rate in the Pacific beetle cockroach, *Diploptera punctata* (Eschscholtz). *J. Exp. Biol.* *210*, 2540–2547.
10. Konduru, S.S., Pan, Y.Z., Wallace, E., Pfammatter, J.A., Jones, M.V., and Maganti, R.K. (2021). Sleep deprivation exacerbates seizures and diminishes GABAergic tonic inhibition. *Ann. Neurol.* *90*, 840–844.
11. Rechtschaffen, A., Gilliland, M.A., Bergmann, B.M., and Winter, J.B. (1983). Physiological correlates of prolonged sleep deprivation in rats. *Science* *221*, 182–184. <https://doi.org/10.1126/science.6857280>.
12. Everson, C.A., Bergmann, B.M., and Rechtschaffen, A. (1989). Sleep deprivation in the rat: III. Total sleep deprivation. *Sleep* *12*, 13–21.
13. Bentivoglio, M., and Grassi-Zucconi, G. (1997). The pioneering experimental studies on sleep deprivation. *Sleep* *20*, 570–576. <https://doi.org/10.1093/sleep/20.7.570>.
14. Besedovsky, L., Lange, T., and Haack, M. (2019). The sleep-immune crosstalk in health and disease. *Physiol. Rev.* *99*, 1325–1380. <https://doi.org/10.1152/physrev.00010.2018>.
15. Chattu, V.K., Manzar, M.D., Kumary, S., Burman, D., Spence, D.W., and Pandi-Perumal, S.R. (2018). The global problem of insufficient sleep and its serious public health implications. *Healthcare (Basel)* *7*, 1. <https://doi.org/10.3390/healthcare7010001>.
16. Prather, A.A., and Leung, C.W. (2016). Association of insufficient sleep with respiratory infection among adults in the United States. *JAMA Intern. Med.* *176*, 850–852. <https://doi.org/10.1001/jamainternmed.2016.0787>.
17. Ranjbaran, Z., Keefer, L., Stepanski, E., Farhadi, A., and Keshavarzian, A. (2007). The relevance of sleep abnormalities to chronic inflammatory conditions. *Inflamm. Res.* *56*, 51–57. <https://doi.org/10.1007/s00011-006-6067-1>.
18. Mullington, J.M., Simpson, N.S., Meier-Ewert, H.K., and Haack, M. (2010). Sleep loss and inflammation. *Best Pract. Res. Clin. Endocrinol. Metab.* *24*, 775–784. <https://doi.org/10.1016/j.beem.2010.08.014>.
19. Musiek, E.S., and Holtzman, D.M. (2016). Mechanisms linking circadian clocks, sleep, and neurodegeneration. *Science* *354*, 1004–1008. <https://doi.org/10.1126/science.aah4968>.
20. Clark, I.A., and Vissel, B. (2014). Inflammation-sleep interface in brain disease: TNF, insulin, orexin. *J. Neuroinflammation* *11*, 51. <https://doi.org/10.1186/1742-2094-11-51>.
21. Everson, C.A., Henchen, C.J., Szabo, A., and Hogg, N. (2014). Cell injury and repair resulting from sleep loss and sleep recovery in laboratory rats. *Sleep* *37*, 1929–1940. <https://doi.org/10.5665/sleep.4244>.
22. Irwin, M.R., and Opp, M.R. (2017). Sleep health: reciprocal regulation of sleep and innate immunity. *Neuropsychopharmacology* *42*, 129–155. <https://doi.org/10.1038/npp.2016.148>.
23. Reynolds, A.C., and Banks, S. (2010). Total sleep deprivation, chronic sleep restriction and sleep disruption. *Prog. Brain Res.* *185*, 91–103. <https://doi.org/10.1016/B978-0-444-53702-7.00006-3>.
24. Colavito, V., Fabene, P.F., Grassi-Zucconi, G., Pifferi, F., Lambert, Y., Bentivoglio, M., and Bertini, G. (2013). Experimental sleep deprivation as a tool to test memory deficits in rodents. *Front. Syst. Neurosci.* *7*, 106. <https://doi.org/10.3389/fnsys.2013.00106>.
25. Borbély, A.A., and Neuhaus, H.U. (1979). Sleep-deprivation: effects on sleep and EEG in the rat. *J. Comp. Physiol.* *133*, 71–87.
26. Van Huizen, Z.J., and Coenen, A.M. (1981). Paradoxical sleep deprivation and locomotor activity in rats. *Physiol. Behav.* *27*, 741–744.
27. Machado, R.B., Hipólido, D.C., Benedito-Silva, A.A., and Tufik, S. (2004). Sleep deprivation induced by the modified multiple platform technique: quantification of sleep loss and recovery. *Brain Res.* *1004*, 45–51. <https://doi.org/10.1016/j.brainres.2004.01.019>.
28. Borbély, A.A. (1982). A two process model of sleep regulation. *Hum. Neurobiol.* *1*, 195–204.
29. Daan, S., Beersma, D.G., and Borbély, A.A. (1984). Timing of human sleep: recovery process gated by a circadian pacemaker. *Am. J. Physiol.* *246*, R161–R183. <https://doi.org/10.1152/ajpregu.1984.246.2.R161>.
30. Allada, R., Cirelli, C., and Sehgal, A. (2017). Molecular mechanisms of sleep homeostasis in flies and mammals. *Cold Spring Harb. Perspect. Biol.* *9*, a027730. <https://doi.org/10.1101/cshperspect.a027730>.
31. Ramírez, M. (2013). Multiple organ dysfunction syndrome. *Curr. Probl. Pediatr. Adolesc. Health Care* *43*, 273–277. <https://doi.org/10.1016/j.cppeds.2013.10.003>.
32. Bitto, A., Polito, F., Altavilla, D., Irrera, N., Giuliani, D., Ottani, A., Minutoli, L., Spaccapelo, L., Galantucci, M., Lodi, R., et al. (2011). Melanocortins protect against multiple organ dysfunction syndrome in mice. *Br. J. Pharmacol.* *162*, 917–928. <https://doi.org/10.1111/j.1476-5381.2010.01098.x>.
33. Karki, R., Sharma, B.R., Tuladhar, S., Williams, E.P., Zalduondo, L., Samir, P., Zheng, M., Sundaram, B., Banoth, B., Malireddi, R.K.S., et al. (2021). Synergism of TNF-alpha and IFN-gamma triggers inflammatory cell death, tissue damage, and mortality in SARS-CoV-2 infection and cytokine shock syndromes. *Cell* *184*, 149–168.e17. <https://doi.org/10.1016/j.cell.2020.11.025>.
34. Mittal, M., Siddiqui, M.R., Tran, K., Reddy, S.P., and Malik, A.B. (2014). Reactive oxygen species in inflammation and tissue injury. *Antioxid. Redox Signal.* *20*, 1126–1167. <https://doi.org/10.1089/ars.2012.5149>.
35. Ho, E., Karimi Galougahi, K., Liu, C.C., Bhindi, R., and Figtree, G.A. (2013). Biological markers of oxidative stress: applications to cardiovascular research and practice. *Redox Biol.* *1*, 483–491.
36. Packer, L., Witt, E.H., and Tritschler, H.J. (1995). Alpha-lipoic acid as a biological antioxidant. *Free Radic. Biol. Med.* *19*, 227–250. [https://doi.org/10.1016/0891-5849\(95\)00017-R](https://doi.org/10.1016/0891-5849(95)00017-R).
37. Aldini, G., Altomare, A., Baron, G., Vistoli, G., Carini, M., Borsani, L., and Sergio, F. (2018). N-acetylcysteine as an antioxidant and disulphide breaking agent: the reasons why. *Free Radical Res.* *52*, 751–762.
38. Tisoncik, J.R., Korth, M.J., Simmons, C.P., Farrar, J., Martin, T.R., and Katze, M.G. (2012). Into the eye of the cytokine storm. *Microbiol. Mol. Biol. Rev.* *76*, 16–32. <https://doi.org/10.1128/MMBR.05015-11>.
39. Fajgenbaum, D.C., Longo, D.L., and June, C.H. (2020). Cytokine storm. *N. Engl. J. Med.* *383*, 2255–2273. <https://doi.org/10.1056/NEJMr2026131>.
40. De Filippo, K., Dudeck, A., Hasenberg, M., Nye, E., van Rooijen, N., Hartmann, K., Gunzer, M., Roers, A., and Hogg, N. (2013). Mast cell and macrophage chemokines CXCL1/CXCL2 control the early stage of neutrophil recruitment during tissue inflammation. *Blood* *121*, 4930–4937. <https://doi.org/10.1182/blood-2013-02-486217>.
41. Girbl, T., Lenn, T., Perez, L., Rolas, L., Barkaway, A., Thriot, A., Del Fresno, C., Lynam, E., Hub, E., Thelen, M., et al. (2018). Distinct compartmentalization of the chemokines CXCL1 and CXCL2 and the atypical receptor ACKR1 determine discrete stages of neutrophil diapedesis. *Immunity* *49*, 1062–1076.e6. <https://doi.org/10.1016/j.immuni.2018.09.018>.
42. Kao, C.Y., Huang, F., Chen, Y., Thai, P., Wachi, S., Kim, C., Tam, L., and Wu, R. (2005). Up-regulation of CC chemokine ligand 20 expression in human airway epithelium by IL-17 through a JAK-independent but MEK/NF-kappaB-dependent signaling pathway. *J. Immunol.* *175*, 6676–6685. <https://doi.org/10.4049/jimmunol.175.10.6676>.
43. Bhattacharya, S., Dunn, P., Thomas, C.G., Smith, B., Schaefer, H., Chen, J., Hu, Z., Zalocusky, K.A., Shankar, R.D., Shen-Orr, S.S., et al. (2018). ImmPort, toward repurposing of open access immunological assay

- data for translational and clinical research. *Sci. Data* 5, 180015. <https://doi.org/10.1038/sdata.2018.15>.
44. Li, H., and Yang, P. (2022). Identification of biomarkers related to neutrophils and two molecular subtypes of systemic lupus erythematosus. *BMC Med. Genomics* 15, 162. <https://doi.org/10.1186/s12920-022-01306-9>.
 45. Frey, N.V., and Porter, D.L. (2016). Cytokine release syndrome with novel therapeutics for acute lymphoblastic leukemia. *Hematology Am. Soc. Hematol. Educ. Program* 2016, 567–572. <https://doi.org/10.1182/asheducation-2016.1.567>.
 46. Henderson, L.A., Canna, S.W., Schulert, G.S., Volpi, S., Lee, P.Y., Kernan, K.F., Caricchio, R., Mahmud, S., Hazen, M.M., Halyabar, O., et al. (2020). On the alert for cytokine storm: immunopathology in COVID-19. *Arthritis Rheumatol.* 72, 1059–1063. <https://doi.org/10.1002/art.41285>.
 47. Shultz, L.D., Lyons, B.L., Burzenski, L.M., Gott, B., Chen, X., Chaleff, S., Kotb, M., Gillies, S.D., King, M., Mangada, J., et al. (2005). Human lymphoid and myeloid cell development in NOD/LtSz-scid IL2R gamma null mice engrafted with mobilized human hemopoietic stem cells. *J. Immunol.* 174, 6477–6489. <https://doi.org/10.4049/jimmunol.174.10.6477>.
 48. Poller, W.C., Downey, J., Mooslechner, A.A., Khan, N., Li, L., Chan, C.T., McAlpine, C.S., Xu, C., Kahles, F., He, S., et al. (2022). Brain motor and fear circuits regulate leukocytes during acute stress. *Nature* 607, 578–584. <https://doi.org/10.1038/s41586-022-04890-z>.
 49. Nauseef, W.M., and Borregaard, N. (2014). Neutrophils at work. *Nat. Immunol.* 15, 602–611. <https://doi.org/10.1038/ni.2921>.
 50. Coutrot, A., Lazar, A.S., Richards, M., Manley, E., Wiener, J.M., Dalton, R.C., Hornberger, M., and Spiers, H.J. (2022). Reported sleep duration reveals segmentation of the adult life-course into three phases. *Nat. Commun.* 13, 7697.
 51. Ford, E.S., Cunningham, T.J., and Croft, J.B. (2015). Trends in self-reported sleep duration among US adults from 1985 to 2012. *Sleep* 38, 829–832.
 52. Daley, J.M., Thomay, A.A., Connolly, M.D., Reichner, J.S., and Albina, J.E. (2008). Use of Ly6G-specific monoclonal antibody to deplete neutrophils in mice. *J. Leukoc. Biol.* 83, 64–70. <https://doi.org/10.1189/jlb.0407247>.
 53. Chiu, S., and Bharat, A. (2016). Role of monocytes and macrophages in regulating immune response following lung transplantation. *Curr. Opin. Organ Transplant.* 21, 239–245. <https://doi.org/10.1097/MOT.0000000000000313>.
 54. Coperchini, F., Chiovato, L., and Rotondi, M. (2021). Interleukin-6, CXCL10 and infiltrating macrophages in COVID-19-related cytokine storm: not one for all but all for one!. *Front. Immunol.* 12, 668507. <https://doi.org/10.3389/fimmu.2021.668507>.
 55. Kreisel, D., Nava, R.G., Li, W., Zinselmeyer, B.H., Wang, B., Lai, J., Pless, R., Gelman, A.E., Krupnick, A.S., and Miller, M.J. (2010). In vivo two-photon imaging reveals monocyte-dependent neutrophil extravasation during pulmonary inflammation. *Proc. Natl. Acad. Sci. USA* 107, 18073–18078. <https://doi.org/10.1073/pnas.1008737107>.
 56. Krause, A.J., Simon, E.B., Mander, B.A., Greer, S.M., Saletin, J.M., Goldstein-Piekarski, A.N., and Walker, M.P. (2017). The sleep-deprived human brain. *Nat. Rev. Neurosci.* 18, 404–418. <https://doi.org/10.1038/nrn.2017.55>.
 57. Zhang, S.L., Lahens, N.F., Yue, Z., Arnold, D.M., Pakstis, P.P., Schwarz, J.E., and Sehgal, A. (2021). A circadian clock regulates efflux by the blood-brain barrier in mice and human cells. *Nat. Commun.* 12, 617. <https://doi.org/10.1038/s41467-020-20795-9>.
 58. Fischer, S., Klüver, N., Burkhardt-Medicke, K., Pietsch, M., Schmidt, A.M., Wellner, P., Schirmer, K., and Luckenbach, T. (2013). Abcb4 acts as multixenobiotic transporter and active barrier against chemical uptake in zebrafish (*Danio rerio*) embryos. *BMC Biol.* 11, 69. <https://doi.org/10.1186/1741-7007-11-69>.
 59. Zhang, S.L., Yue, Z., Arnold, D.M., Artiushin, G., and Sehgal, A. (2018). A circadian clock in the blood-brain barrier regulates xenobiotic efflux. *Cell* 173, 130–139.e10. <https://doi.org/10.1016/j.cell.2018.02.017>.
 60. Hawkins, B.T., Sykes, D.B., and Miller, D.S. (2010). Rapid, reversible modulation of blood-brain barrier P-glycoprotein transport activity by vascular endothelial growth factor. *J. Neurosci.* 30, 1417–1425. <https://doi.org/10.1523/JNEUROSCI.5103-09.2010>.
 61. Zhao, Z., Nelson, A.R., Betsholtz, C., and Zlokovic, B.V. (2015). Establishment and dysfunction of the blood-brain barrier. *Cell* 163, 1064–1078.
 62. Graham, G.G., Davies, M.J., Day, R.O., Mohamudally, A., and Scott, K.F. (2013). The modern pharmacology of paracetamol: therapeutic actions, mechanism of action, metabolism, toxicity and recent pharmacological findings. *Inflammopharmacology* 21, 201–232. <https://doi.org/10.1007/s10787-013-0172-x>.
 63. Kantrowitz, F., Robinson, D.R., McGuire, M.B., and Levine, L. (1975). Corticosteroids inhibit prostaglandin production by rheumatoid synovia. *Nature* 258, 737–739. <https://doi.org/10.1038/258737a0>.
 64. Urade, Y., and Hayaishi, O. (2011). Prostaglandin D2 and sleep/wake regulation. *Sleep Med. Rev.* 15, 411–418. <https://doi.org/10.1016/j.smrv.2011.08.003>.
 65. Qu, W.M., Huang, Z.L., Xu, X.H., Aritake, K., Eguchi, N., Nambu, F., Narumiya, S., Urade, Y., and Hayaishi, O. (2006). Lipocalin-type prostaglandin D synthase produces prostaglandin D2 involved in regulation of physiological sleep. *Proc. Natl. Acad. Sci. USA* 103, 17949–17954. <https://doi.org/10.1073/pnas.0608581103>.
 66. Urade, Y., Kitahama, K., Ohishi, H., Kaneko, T., Mizuno, N., and Hayaishi, O. (1993). Dominant expression of mRNA for prostaglandin D synthase in leptomeninges, choroid plexus, and oligodendrocytes of the adult rat brain. *Proc. Natl. Acad. Sci. USA* 90, 9070–9074. <https://doi.org/10.1073/pnas.90.19.9070>.
 67. Mizoguchi, A., Eguchi, N., Kimura, K., Kiyohara, Y., Qu, W.M., Huang, Z.L., Mochizuki, T., Lazarus, M., Kobayashi, T., Kaneko, T., et al. (2001). Dominant localization of prostaglandin D receptors on arachnoid trabecular cells in mouse basal forebrain and their involvement in the regulation of non-rapid eye movement sleep. *Proc. Natl. Acad. Sci. USA* 98, 11674–11679. <https://doi.org/10.1073/pnas.201398898>.
 68. Scammell, T.E., Gerashchenko, D.Y., Mochizuki, T., McCarthy, M.T., Estabrooke, I.V., Sears, C.A., Saper, C.B., Urade, Y., and Hayaishi, O. (2001). An adenosine A2a agonist increases sleep and induces Fos in ventrolateral preoptic neurons. *Neuroscience* 107, 653–663. [https://doi.org/10.1016/s0306-4522\(01\)00383-9](https://doi.org/10.1016/s0306-4522(01)00383-9).
 69. Gallopin, T., Luppi, P.H., Cauli, B., Urade, Y., Rossier, J., Hayaishi, O., Lambollez, B., and Fort, P. (2005). The endogenous somnogen adenosine excites a subset of sleep-promoting neurons via A2A receptors in the ventrolateral preoptic nucleus. *Neuroscience* 134, 1377–1390. <https://doi.org/10.1016/j.neuroscience.2005.05.045>.
 70. Ricciotti, E., and FitzGerald, G.A. (2011). Prostaglandins and inflammation. *Arterioscler. Thromb. Vasc. Biol.* 31, 986–1000. <https://doi.org/10.1161/ATVBAHA.110.207449>.
 71. Woodward, D.F., Jones, R.L., and Narumiya, S. (2011). International union of basic and Clinical Pharmacology. LXXXIII: classification of prostanoicid receptors, updating 15 years of progress. *Pharmacol. Rev.* 63, 471–538. <https://doi.org/10.1124/pr.110.003517>.
 72. Jing, M., Zhang, Y., Wang, H., and Li, Y. (2019). G-protein-coupled receptor-based sensors for imaging neurochemicals with high sensitivity and specificity. *J. Neurochem.* 151, 279–288. <https://doi.org/10.1111/jnc.14855>.
 73. Wan, J., Peng, W., Li, X., Qian, T., Song, K., Zeng, J., Deng, F., Hao, S., Feng, J., Zhang, P., et al. (2021). A genetically encoded sensor for measuring serotonin dynamics. *Nat. Neurosci.* 24, 746–752. <https://doi.org/10.1038/s41593-021-00823-7>.
 74. Dong, H., Li, M., Yan, Y., Qian, T., Lin, Y., Ma, X., Vischer, H.F., Liu, C., Li, G., Wang, H., et al. (2023). Genetically encoded sensors for measuring

- histamine release both in vitro and in vivo. *Neuron* 111, 1564–1576.e6. <https://doi.org/10.1016/j.neuron.2023.02.024>.
75. Sun, F., Zhou, J., Dai, B., Qian, T., Zeng, J., Li, X., Zhuo, Y., Zhang, Y., Wang, Y., Qian, C., et al. (2020). Next-generation GRAB sensors for monitoring dopaminergic activity in vivo. *Nat. Methods* 17, 1156–1166. <https://doi.org/10.1038/s41592-020-00981-9>.
 76. Wang, H., Qian, T., Zhao, Y., Zhuo, Y., Wu, C., Osakada, T., Chen, P., Ren, H., Yan, Y., and Geng, L. (2022). A toolkit of highly selective and sensitive genetically encoded neuropeptide sensors. <https://doi.org/10.1101/2022.03.26.485911>.
 77. Kiriya, M., Ushikubi, F., Kobayashi, T., Hirata, M., Sugimoto, Y., and Narumiya, S. (1997). Ligand binding specificities of the eight types and subtypes of the mouse prostanoid receptors expressed in Chinese hamster ovary cells. *Br. J. Pharmacol.* 122, 217–224. <https://doi.org/10.1038/sj.bjpp.0701367>.
 78. Matsumura, H., Nakajima, T., Osaka, T., Satoh, S., Kawase, K., Kubo, E., Kantha, S.S., Kasahara, K., and Hayaishi, O. (1994). Prostaglandin D₂-sensitive, sleep-promoting zone defined in the ventral surface of the rostral basal forebrain. *Proc. Natl. Acad. Sci. USA* 91, 11998–12002.
 79. Wang, T.A., Teo, C.F., Åkerblom, M., Chen, C., Tynan-La Fontaine, M., Greiner, V.J., Diaz, A., McManus, M.T., Jan, Y.N., and Jan, L.Y. (2019). Thermoregulation via temperature-dependent PGD(2) production in mouse preoptic area. *Neuron* 103, 309–322.e307. <https://doi.org/10.1016/j.neuron.2019.04.035>.
 80. Pettipher, R., Hansel, T.T., and Armer, R. (2007). Antagonism of the prostaglandin D₂ receptors DP1 and CRTH2 as an approach to treat allergic diseases. *Nat. Rev. Drug Discov.* 6, 313–325.
 81. Song, W.L., Wang, M., Ricciotti, E., Fries, S., Yu, Y., Grosser, T., Reilly, M., Lawson, J.A., and FitzGerald, G.A. (2008). Tetranor PGDM, an abundant urinary metabolite reflects biosynthesis of prostaglandin D₂ in mice and humans. *J. Biol. Chem.* 283, 1179–1188. <https://doi.org/10.1074/jbc.M706839200>.
 82. Liu, M., Liu, H., Li, F., Shen, Y., Zhang, L., Wang, G., Wang, H., Qu, C., Chen, G., Zhao, X., et al. (2023). Metagenomic surveillance in Jinan, China, reveals serum microbiome and biochemistry features in fever of unknown origin (FUO) patients. *Lett. Appl. Microbiol.* 76, ovad060.
 83. Reid, G., Wielinga, P., Zelcer, N., van der Heijden, I., Kuil, A., de Haas, M., Wijnholds, J., and Borst, P. (2003). The human multidrug resistance protein MRP4 functions as a prostaglandin efflux transporter and is inhibited by nonsteroidal antiinflammatory drugs. *Proc. Natl. Acad. Sci. USA* 100, 9244–9249. <https://doi.org/10.1073/pnas.1033060100>.
 84. Akanuma, S.I., Hashimoto, K., Yoshida, Y., Kubo, Y., and Hosoya, K.I. (2020). Inflammation-induced attenuation of prostaglandin D₂ elimination across rat blood-brain barrier: involvement of the downregulation of organic anion transporter 3 and multidrug resistance-associated Protein 4. *Biol. Pharm. Bull.* 43, 1669–1677. <https://doi.org/10.1248/bpb.b20-00388>.
 85. Kakee, A., Terasaki, T., and Sugiyama, Y. (1996). Brain efflux index as a novel method of analyzing efflux transport at the blood-brain barrier. *J. Pharmacol. Exp. Ther.* 277, 1550–1559.
 86. Wang, G., Li, Q., Xu, J., Zhao, S., Zhou, R., Chen, Z., Jiang, W., Gao, X., Zhou, S., Chen, Z., et al. (2022). Somatic genetics analysis of sleep in adult mice. *J. Neurosci.* 42, 5617–5640. <https://doi.org/10.1523/JNEUROSCI.0089-22.2022>.
 87. Zhou, R., Wang, G., Li, Q., Meng, F., Liu, C., Gan, R., Ju, D., Liao, M., Xu, J., Sang, D., et al. (2022). A signalling pathway for transcriptional regulation of sleep amount in mice. *Nature* 612, 519–527. <https://doi.org/10.1038/s41586-022-05510-6>.
 88. Rittirsch, D., Huber-Lang, M.S., Flierl, M.A., and Ward, P.A. (2009). Immunomodulation of experimental sepsis by cecal ligation and puncture. *Nat. Protoc.* 4, 31–36. <https://doi.org/10.1038/nprot.2008.214>.
 89. Toscano, M.G., Ganea, D., and Gamero, A.M. (2011). Cecal ligation puncture procedure. *J. Vis. Exp.* 2860. <https://doi.org/10.3791/2860>.
 90. Zamore, Z., and Veasey, S.C. (2022). Neural consequences of chronic sleep disruption. *Trends Neurosci.* 45, 678–691. <https://doi.org/10.1016/j.tins.2022.05.007>.
 91. Owens, D.J., Twist, C., Cobley, J.N., Howatson, G., and Close, G.L. (2019). Exercise-induced muscle damage: what is it, what causes it and what are the nutritional solutions? *Eur. J. Sport Sci.* 19, 71–85. <https://doi.org/10.1080/17461391.2018.1505957>.
 92. Peake, J.M., Neubauer, O., Della Gatta, P.A., and Nosaka, K. (2017). Muscle damage and inflammation during recovery from exercise. *J. Appl. Physiol.* (1985) 122, 559–570.
 93. Ahmad, A.S., Ottallah, H., Maciel, C.B., Strickland, M., and Doré, S. (2019). Role of the L-PGDS-PGD2-DP1 receptor axis in sleep regulation and neurological outcomes. *Sleep* 42, zsz073. <https://doi.org/10.1093/sleep/zsz073>.
 94. Bate, C., Kempster, S., and Williams, A. (2006). Prostaglandin D₂ mediates neuronal damage by amyloid-beta or prions which activates microglial cells. *Neuropharmacology* 50, 229–237. <https://doi.org/10.1016/j.neuropharm.2005.09.008>.
 95. Zhao, H., Ohinata, K., and Yoshikawa, M. (2009). Central prostaglandin D₂ exhibits anxiolytic-like activity via the DP(1) receptor in mice. *Prostaglandins Other Lipid Mediat.* 88, 68–72. <https://doi.org/10.1016/j.prostaglandins.2008.10.001>.
 96. Hayaishi, O., Urade, Y., Eguchi, N., and Huang, Z.-L. (2004). Genes for prostaglandin D synthase and receptor as well as adenosine A_{2a} receptor are involved in the homeostatic regulation of NREM sleep. *Arch. Ital. Biol.* 142, 533–539.
 97. Spik, I., Brénuçon, C., Angéli, V., Stumont, D., Fleury, S., Capron, M., Trottein, F., and Dombrowicz, D. (2005). Activation of the prostaglandin D₂ receptor DP2/CRTH2 increases allergic inflammation in mouse. *J. Immunol.* 174, 3703–3708.
 98. Satoh, T., Moroi, R., Aritake, K., Urade, Y., Kanai, Y., Sumi, K., Yokozeki, H., Hirai, H., Nagata, K., and Hara, T. (2006). Prostaglandin D₂ plays an essential role in chronic allergic inflammation of the skin via CRTH2 receptor. *J. Immunol.* 177, 2621–2629.
 99. Seugnet, L., Suzuki, Y., Donlea, J.M., Gottschalk, L., and Shaw, P.J. (2011). Sleep deprivation during early-adult development results in long-lasting learning deficits in adult *Drosophila*. *Sleep* 34, 137–146. <https://doi.org/10.1093/sleep/34.2.137>.
 100. Zhu, Y., Fenik, P., Zhan, G., Somach, R., Xin, R., and Veasey, S. (2016). Intermittent short sleep results in lasting sleep wake disturbances and degeneration of locus coeruleus and orexinergic neurons. *Sleep* 39, 1601–1611. <https://doi.org/10.5665/sleep.6030>.
 101. Davies, S.K., Ang, J.E., Revell, V.L., Holmes, B., Mann, A., Robertson, F.P., Cui, N., Middleton, B., Ackermann, K., Kayser, M., et al. (2014). Effect of sleep deprivation on the human metabolome. *Proc. Natl. Acad. Sci. USA* 111, 10761–10766. <https://doi.org/10.1073/pnas.1402663111>.
 102. Liu, H., and Chen, A. (2019). Roles of sleep deprivation in cardiovascular dysfunctions. *Life Sci.* 219, 231–237. <https://doi.org/10.1016/j.lfs.2019.01.006>.
 103. Simpson, N.S., DiIombi, M., Scott-Sutherland, J., Yang, H., Bhatt, V., Gautam, S., Mullington, J., and Haack, M. (2016). Repeating patterns of sleep restriction and recovery: do we get used to it? *Brain Behav. Immun.* 58, 142–151. <https://doi.org/10.1016/j.bbi.2016.06.001>.
 104. Culemann, S., Knab, K., Euler, M., Wegner, A., Garibagaoglu, H., Ackermann, J., Fischer, K., Kienhöfer, D., Crainiciuc, G., Hahn, J., et al. (2023). Stunning of neutrophils accounts for the anti-inflammatory effects of clodronate liposomes. *J. Exp. Med.* 220, e20220525. <https://doi.org/10.1084/jem.20220525>.
 105. Sanjana, N.E., Shalem, O., and Zhang, F. (2014). Improved vectors and genome-wide libraries for CRISPR screening. *Nat. Methods* 11, 783–784. <https://doi.org/10.1038/nmeth.3047>.
 106. Barger, Z., Frye, C.G., Liu, D., Dan, Y., and Bouchard, K.E. (2019). Robust, automated sleep scoring by a compact neural network with

- distributional shift correction. *PLoS One* 14, e0224642. <https://doi.org/10.1371/journal.pone.0224642>.
107. Schindelin, J., Arganda-Carreras, I., Frise, E., Kaynig, V., Longair, M., Pietzsch, T., Preibisch, S., Rueden, C., Saalfeld, S., and Schmid, B. (2012). Fiji: an open-source platform for biological-image analysis. *Nat. Methods* 9, 676–682.
 108. Bolger, A.M., Lohse, M., and Usadel, B. (2014). Trimmomatic: a flexible trimmer for Illumina sequence data. *Bioinformatics* 30, 2114–2120.
 109. Dobin, A., Davis, C.A., Schlesinger, F., Drenkow, J., Zaleski, C., Jha, S., Batut, P., Chaisson, M., and Gingeras, T.R. (2013). STAR: ultrafast universal RNA-seq aligner. *Bioinformatics* 29, 15–21.
 110. Liao, Y., Smyth, G.K., and Shi, W. (2014). featureCounts: an efficient general purpose program for assigning sequence reads to genomic features. *Bioinformatics* 30, 923–930.
 111. Stuart, T., Butler, A., Hoffman, P., Hafemeister, C., Papalexi, E., Mauck, W.M., Hao, Y., Stoeckius, M., Smibert, P., and Satija, R. (2019). Comprehensive integration of single-cell data. *Cell* 177, 1888–1902.e21.
 112. Kuleshov, M.V., Jones, M.R., Rouillard, A.D., Fernandez, N.F., Duan, Q., Wang, Z., Koplev, S., Jenkins, S.L., Jagodnik, K.M., Lachmann, A., et al. (2016). Enrichr: a comprehensive gene set enrichment analysis web server 2016 update. *Nucleic Acids Res.* 44, W90–W97. <https://doi.org/10.1093/nar/gkw377>.
 113. Farkas, A.E., Gerner-Smidt, C., Lili, L., Nusrat, A., and Capaldo, C.T. (2015). Cryosectioning method for microdissection of murine colonic mucosa. *J. Vis. Exp.* e53112. <https://doi.org/10.3791/53112>.
 114. Janssen, H., Kahles, F., Liu, D., Downey, J., Koekkoek, L.L., Roudko, V., D'Souza, D., McAlpine, C.S., Halle, L., and Poller, W.C. (2023). Monocytes re-enter the bone marrow during fasting and alter the host response to infection. *Immunity* 56, 783–796.e7.
 115. Andreato, F., Blériot, C., Di Lucia, P., De Simone, G., Fumagalli, V., Ficht, X., Beccaria, C.G., Kuka, M., Ginhoux, F., and Iannaccone, M. (2021). Isolation of mouse Kupffer cells for phenotypic and functional studies. *STAR Protoc.* 2, 100831.
 116. Boulay, A.C., Saubaméa, B., Declèves, X., and Cohen-Salmon, M. (2015). Purification of mouse brain vessels. *J. Vis. Exp.* e53208. <https://doi.org/10.3791/53208>.
 117. Akanuma, S., Hosoya, K., Ito, S., Tachikawa, M., Terasaki, T., and Ohtsuki, S. (2010). Involvement of multidrug resistance-associated protein 4 in efflux transport of prostaglandin E(2) across mouse blood-brain barrier and its inhibition by intravenous administration of cephalosporins. *J. Pharmacol. Exp. Ther.* 333, 912–919. <https://doi.org/10.1124/jpet.109.165332>.
 118. Feng, J., Zhang, C., Lischinsky, J.E., Jing, M., Zhou, J., Wang, H., Zhang, Y., Dong, A., Wu, Z., and Wu, H. (2019). A genetically encoded fluorescent sensor for rapid and specific in vivo detection of norepinephrine. *Neuron* 102, 745–761.e8.

STAR★METHODS

KEY RESOURCES TABLE

REAGENT or RESOURCE	SOURCE	IDENTIFIER
Antibodies		
<i>InVivo</i> MAb anti-mouse Ly6G (clone 1A8)	BioXCell	Cat#BE0075-1; RRID: AB_1107721
<i>InVivo</i> Mab rat IgG2a isotype control (clone 2A3)	BioXCell	Cat#BE0089; RRID: AB_1107769
APC anti-mouse/human CD11b Antibody (clone M1/70)	BioLegend	Cat#101212; RRID: AB_312795
PE anti-mouse Ly-6G Antibody (clone1A8)	BioLegend	Cat#127608; RRID: AB_1186099
FITC anti-mouse CD45 Antibody (clone 30-F11)	BioLegend	Cat#103108; RRID: AB_312973
APC anti-mouse CD115 Antibody (clone AFS98)	BioLegend	Cat# 135510; RRID: AB_2085221
Ly-6G/Ly-6C Monoclonal Antibody (clone RB6-8C5)	eBioscience	Cat#14-5931-82; RRID: AB_467730
APC anti-mouse F4/80 Antibody (clone BM8)	eBioscience	Cat#123115; RRID: AB_893493
Goat anti-Rat IgG (H+L) (Alexa Fluor™ Plus 555)	Invitrogen	Cat# A48263; RRID: AB_2896332
Purified Rat Anti-Mouse CD31 (clone MEC13.3(RUO))	BD Biosciences	Cat#553370; RRID: AB_396660
Goat Anti-Rat IgG H&L (Alexa Fluor® 488)	Abcam	Cat# ab150157; RRID: AB_2722511
Recombinant Anti-Prostaglandin D Synthase (Lipocalin)/PDS antibody [EP12357]	Abcam	Cat# ab182141; RRID: AB_2783784
Anti-rabbit IgG, HRP-linked Antibody	Cell Signaling Technology	Cat#7074; RRID: AB_2099233
Beta Actin Monoclonal antibody (clone 2D4H5)	Proteintech	Cat# 66009-1-Ig; RRID: AB_2687938
Anti-mouse IgG, HRP-linked Antibody	Cell Signaling Technology	Cat#7076; RRID: AB_330924
Bacterial and virus strains		
AAV-PHP.eB-3xsgRNA ^{Ptgds}	This paper	N/A
AAV-PHP.eB-3xsgRNA ^{NT}	This paper	N/A
AAV2/9-hSyn-GRAB _{PGD2-1.0}	This paper	N/A
AAV9-EF1 α -GRAB _{PGD2-1.1}	This paper	N/A
Chemicals, peptides, and recombinant proteins		
Acetaminophen	MedChem Express	Cat#HY-66005; CAS: 103-90-2
Corticosterone	MedChem Express	Cat#HY-B1618; CAS: 50-22-6
MK-571 sodium	MedChem Express	Cat#HY-19989A; CAS: 115103-85-0
Lipoic acid	MedChem Express	Cat#HY-18733; CAS: 1200-22-2
N-Acetyl-cysteine	Sigma-Aldrich	Cat#V900429; CAS: 616-91-1
Tariquidar	MedChem Express	Cat#HY-10550; CAS: 206873-63-4
L 888607	MedChem Express	Cat#HY-111271; CAS: 860033-06-3
Treprostinil sodium	MedChem Express	Cat#HY-16504; CAS: 289480-64-4
Asapirant	MedChem Express	Cat# HY-16763; CAS: 932372-01-5
Prostalandin E2	MedChem Express	Cat#HY-101952; CAS: 363-24-6
Prostalandin D2	Sigma-Aldrich	Cat#P5172; CAS: 41598-07-6
Prostaglandin D2, [5,6,8,9,12,14,15-3H(N)]-	PerkinElmer	Cat#NET616100UC
Inulin carboxyl [carboxyl-14C]	American Radiolabeled Chemicals	Cat#ARC 0124
Rhodamine B	Sigma-Aldrich	Cat#83689; CAS: 81-88-9
6-Hydroxydopamine hydrobromide	Sigma-Aldrich	Cat#162957; CAS: 636-00-0
D-(+)-Glucose	Merck	Cat#G8270; CAS: 50-99-7
DAPI	Merck	Cat#D9542; CAS: 28718-90-3
Dihydroethidium	Beyotime	Cat#S0063; CAS: 104821-25-2
Percoll	Cytiva	Cat#17089101

(Continued on next page)

Continued

REAGENT or RESOURCE	SOURCE	IDENTIFIER
Clodronate Liposomes	Yeasen	Cat#40337ES08
PEI MAX®	Polyscience	Cat#24765-100
Tetranor-PGDM	Cayman Chemical	Cat# 12850; CAS: 70803-91-7
DMSO	VWR Life Science	Cat# 97061-250; CAS: 67-68-5

Critical commercial assays

One-step TUNEL In Situ Apoptosis Kit (Green, Elab Fluor® 488)	Elabscience	Cat#E-CK-A321
QIAamp RNA Blood Mini Kit	Qiagen	Cat#52304
U-PLEX Biomarker Group 1 (mouse) 35-Plex	Meso Scale Discovery	Cat#K15083K
V-PLEX Proinflammatory Panel 1 Mouse Kit	Meso Scale Discovery	Cat# K15048D-X
Mouse IL-6 Quantikine ELISA Kit	R&D Systems	Cat#M6000B
Corticosterone Parameter Assay Kit	R&D Systems	Cat#KGE009
3' scRNA-seq kit v3 chemistry	10x Genomics	v3 chemistry

Deposited data

Raw and analyzed sequencing data	This paper	GEO: GSE213497
Mouse cytokine and chemokine raw data	This paper	Table S1
Mouse GeCKO v2 Library	Sanjana et al. ¹⁰⁵	http://doi.org/10.1038/nmeth.3047

Experimental models: Cell lines

HEK293T	ATCC	CRL-3216
Rat primary cortical neurons	This paper	N/A

Experimental models: Organisms/strains

Mouse: C57BL/6JNifdc	Vital River	Cat#219
Mouse: C57BL/6NCrl	Vital River	Cat#213
Rat: CD® (SD) IGS	Vital River	Cat#101
Mouse: NOD.Cg-Prkdc ^{scid} Il2rg ^{em1Smoc}	Shanghai Model Organisms	NM-NSG-001; RRID: IMSR_NM-NSG-001
Mouse: B6J.129(Cg)-Gt(ROSA)26Sor ^{tm1.1(CAG-cas9*,-EGFP)Fezh/J}	Jackson Laboratory	026179; RRID: IMSR_JAX:026179
Mouse: C57BL/6JGpt-Ptgds ^{em8Cd8326in1} /Gpt	GemPharmatech	T028417; RRID: IMSR_GPT:T028417
Mouse: C57BL/6JGpt-Abcc4 ^{em37Cd2585} /Gpt	GemPharmatech	T013837; RRID: IMSR_GPT:T013837

Oligonucleotides

Ptgds sgRNA-1: CAGAGCGTACTCGTCATAGT	Sanjana et al. ¹⁰⁵	MGLibA_43606
Ptgds sgRNA-2: GGTCGAGTTCCTGGGGCGC	Sanjana et al. ¹⁰⁵	MGLibA_43607
Ptgds sgRNA-3: TACGCTCTGCTATTGAGCAG	Sanjana et al. ¹⁰⁵	MGLibA_43608
NT sgRNA-1: ACGTGTAAGGCGAACGCCTT	Wang et al. ⁸⁶	N/A
NT sgRNA-2: GACTCCGGTACTAAATGTC	Wang et al. ⁸⁶	N/A
NT sgRNA-3: CCGCGCCGTTAGGGAACGAG	Wang et al. ⁸⁶	N/A

Software and algorithms

AccuSleep	Barger et al. ¹⁰⁶	https://github.com/zekebarger/AccuSleep
ImageJ-Fiji	Schindelin et al. ¹⁰⁷	https://imagej.net/software/fiji/
Prism 9	GraphPad Software	https://www.graphpad.com/scientific-software/prism/
Open Ephys GUI	Open Ephys	https://open-ephys.org/gui
EEG/EMG analysis scripts	This paper	N/A
FastQC v0.11.9	Simon Andrews	https://github.com/s-andrews/FastQC
Trimomatic v0.39	Bolger et al. ¹⁰⁸	https://github.com/usadellab/Trimomatic
STAR v2.7.9a	Dobin et al. ¹⁰⁹	https://github.com/alexdobin/STAR
featureCounts v2.0.3	Liao et al. ¹¹⁰	https://sourceforge.net/projects/subread/files/subread-2.0.3/

(Continued on next page)

Continued

REAGENT or RESOURCE	SOURCE	IDENTIFIER
Cell Ranger v4.0.0	10x Genomics	https://support.10xgenomics.com/single-cell-gene-expression/software/pipelines/latest/installation
R version 4.0.2	R Core	https://www.R-project.org/
Seurat v3.0	Stuart et al. ¹¹¹	https://github.com/satijalab/seurat
Flow Jo v10	BD Biosciences	https://www.flowjo.com/solutions/flowjo/downloads
Other		
Collagenase IV	Sigma-Aldrich	Cat#C5138
DNase I	New England Biolabs	Cat# M0303L
70- μ m cell strainer	Falcon	Cat#352350
Ultima Gold XR	PerkinElmer	Cat#6013111
Super Polyethylene Vial, 20 mL	PerkinElmer	Cat#6001075
StrataX C18 cartridge	Phenomenex	Cat#8B-S100-UAK

RESOURCE AVAILABILITY**Lead contact**

Further information and requests for resources and reagents should be directed to and will be fulfilled by the lead contact, Dr Eric Erquan Zhang (zhangerquan@nibs.ac.cn).

Materials availability

This study did not generate new unique reagents.

Data and code availability

- The raw and processed RNA-seq data and scRNA-seq data have been deposited at the NCBI Gene Expression Omnibus under accession number GSE213497.
- Other data reported in this paper will be shared by the [lead contact](#) upon reasonable request.
- All MATLAB and R scripts used in this manuscript are available from the [lead contact](#) upon reasonable request.
- Any additional information required to reanalyze the data reported in this paper is available from the [lead contact](#) upon request.

EXPERIMENTAL MODEL AND STUDY PARTICIPANT DETAILS**Mice**

All procedures were conducted with the approval of the Institutional Animal Care and Use Committee (IACUC) of the National Institute of Biological Sciences, Beijing in accordance with the governmental regulations of China. Adult mice (8-10 weeks) of either sex were used. All mice were maintained in a standard 12h light: 12h night (LD) photoperiod at 22-25°C with *ad libitum* access to standard chow and water. C57BL/6J mice, C57BL/6N mice, and CD® (SD) IGS rat were purchased from Vital River. M-NSG (NOD-*Prkdc*^{scid}*Il2rg*^{em/Smoc}, stock#NM-NSG-001) mice were purchased from Shanghai Model Organisms Center. Rosa26-Cas9 knockin mice (stock#026179) were purchased from Jackson Laboratory. C57BL/6JGpt-*Ptgds*^{em8Cd8326in1}/Gpt (stock#T028417) and C57BL/6JGpt-*Abcc4*^{em37Cd2585}/Gpt (stock#T013837) mice were purchased from GemPharmatech.

Cell lines

HEK293T and rat primary cortical neurons were used in this study. HEK293T cells were cultured at 37°C, 5% CO₂ in DMEM (Gibco) supplemented with 10% (v/v) fetal bovine serum (Gibco) and 1% penicillin-streptomycin (Gibco). The rat cortical neurons were isolated from postnatal day 0 (P0) Sprague-Dawley rat pups and were cultured in Neurobasal medium (Gibco) supplemented with 2% B-27 (Gibco), 1% GlutaMax (Gibco), and 1% penicillin-streptomycin (Gibco) at 37°C with 5% CO₂.

METHOD DETAILS**Curling Prevention by Water (CPW) paradigm**

A customized acrylic cylinder (20 cm in height and 25 cm in diameter) with a modified cover was used to deprive mice of sleep. Food was provided with the attached food trough, and drinking water was supplied using a rodent water bottle attached to the outside of

the cylinder with the spout inserted inside of the cylinder. Each mouse was singly housed in the bedding filled cylinder (home-cage control condition) to acclimate to the environment for more than 48 h.

For the sleep deprivation (SD) group, distilled water (about 315 mL) at room temperature was used to form an 8-mm deep water layer in the cylinder. The mouse was transferred and housed in the water-covered cylinder at ZT0. For prolonged sleep deprivation, the water-covered cylinder was changed every 24 h to keep a clean environment for the sleep-deprived mice. The replaced cylinder and food trough was cleaned and sterilized with disinfectant solution and ultraviolet light before reuse. During SD, premature mortality occurred, and hours before the mortality, the mice showed difficulties in maintaining balance, little or no reactions to gentle touch, and severe hypothermia. According to the guidance of animal welfare and judgment of veterinarian, these mice facing mortality were euthanized with an overdose of pentobarbital (250 mg/kg). After sleep deprivation, the mice were transferred and housed in home cage control condition with bedding and extra absorbent paper to reduce the interval period of hair grooming before the recovery sleep.

For the environmental control (eCon) group, the same system setup was prepared as described above. One 10-cm culture dish was filled with distilled water to stabilize the culture dish and the cover was wrapped with wet gauze. The gauze covered culture dish was placed opposite to the food trough in the cylinder, so that the mouse could sleep on the wet culture dish.

Stand Alone Sleep Deprivation (SASD) paradigm

For mechanical and automatic sleep deprivation with SASD, mice were placed into a XR-XS108 sleep restriction chamber (Shanghai XinRuan Information Technology) with an intermittently sweeping bar placed 2 cm above the chamber bottom. This kept the mice moving to limit sleep. The bar was programmed to rotate 360 degrees clockwise then 360 degrees counter-clockwise at 10 rpm with a 6-s pause between rotations. The control mice without sleep deprivation were placed into the same sleep restriction chamber without the sweeping setting. Both SASD mice and control mice had *ad libitum* access to chow and water. For each group of SASD mice, 3 mice were placed in each chamber for respective time started from ZT0.

EEG/EMG-based sleep/wake analysis

For EEG/EMG electrode implantation, each 7- to 8-week-old mouse was anesthetized with pentobarbital (*i.p.* 80 mg/kg), and the skull was exposed with surgical scissors and forceps. 5% hydrogen peroxide was used to clean the exposed skull with cotton swabs. Two stainless steel miniscrews that were connected to two electrode pins of the four-pin connector separately with thin coated sliver string were implanted into the skull above the frontal (anterior-posterior (AP) +1.6 mm; medial-lateral (ML) -1.3 mm) and temporal (AP -5.4 mm; ML +1.3 mm), and two EMG recording miniwires that were also connected to the other two electrode pins separately were inserted into the neck muscle. The four-pin connector was mounted on the skull with dental cement. After surgery, the mice were singly housed and recovered for at least 48 h before acclimation in the recording room with the recording wires attach to the four-pin connector.

The sleep stage of the mouse was automatically analyzed by a previously reported machine learning algorithm.¹⁰⁶ Briefly, the EEG and EMG data from Open Ephys GUI were changed format to make it compatible with downstream analysis by the Open Ephys provided script. To remove variability caused by experimental manipulations, a mixture z-scoring parameters were set by manually selecting a few epochs of each sleep stages. Further, a pre-trained basic CNN (Convolutional Neural Networks) was loaded and used for automated sleep stage classification. The following statistical analysis of sleep amount was performed by in-house MATLAB scripts.

Necropsy and histopathology of dead mice

Eight mice in the survival study of prolonged sleep deprivation in C57BL/6J mice were subjected to gross necropsy with a veterinarian. Further histopathology studies were performed. Heart, spleen, liver, lung, small intestine, large intestine, and kidney tissues were fixed in 10% formalin overnight. Hematoxylin and eosin (H&E) stained slides were prepared and reviewed by two independent pathologists (one in China Agriculture University Veterinary Teaching Hospital, the other in Lab Animal Technology Develop Co.), who were blinded to experimental designs and conditions.

H&E staining

Lungs, livers and spleens were fixed with 4% paraformaldehyde (PFA) overnight and paraffin embedded. Sections were cut at 10 μ m. The experiment followed the standard H&E staining protocol. Briefly, after dewaxing and rehydrating, the nuclei were stained by hematoxylin (Sigma, 03971) for 3 min, and differentiated by acid alcohol for 30 s. The cytoplasm was staining by eosin (Sigma, 318906) for 10 s. Slices were dehydrated and sealed with neutral resin. The slices were scanned with an VS120 Virtual Slide Microscope (Olympus Life Sciences).

TUNEL assay

For TUNEL assay of liver tissue sections, 10- μ m paraffin sections were treated according to the instructions of the One-step TUNEL In Situ Apoptosis Kit (Elabscience, E-CK-321). After dewaxing, the slides were immersed in proteinase K for 20min, and washed with PBS 3 times for 5min. 50 μ L of TUNEL reaction mixture was added to the sample, and incubated in a dark and wet box at 37°C for 1h. After washing 3 times with PBS, slides were counterstained with DAPI and mounted in 50% glycerol. The slices were scanned on an VS120 Virtual Slide Microscope (Olympus, VS120-S6-W).

Immunofluorescence staining

Liver tissues were fixed in 4% PFA for 10 h, cryoprotected in 30% sucrose overnight, and then embedded in OCT. 30- μ m cryosections were used for immunofluorescence staining. Sections were blocked with protein block (Abcam, ab64226) at room temperature for 1 hour. Then sections were incubated with rat-anti-Ly6G/Ly6C (1:100, ThermoFisher, 14-5931-82) at 4°C overnight. After washing with DPBS for 3 times, the slices were incubated with Goat anti-Rat IgG (H+L), Alexa Fluor™ Plus 555 (Invitrogen, A48263) diluted at 1:500 for 1 h at room temperature. The nuclei were stained with DAPI, and slides were mounted with 50% glycerol. The slices were scanned on an VS120 Virtual Slide Microscope. The number of neutrophils in the liver was calculated using a 20 \times objective. Five microscope fields, each equivalent to a 4-mm² area, were analyzed for each section. Using the ImageJ software neutrophils were counted manually from immunostaining slides.

Administration of drugs during CPW procedure

Acetaminophen (1.6 mg/mL in ddH₂O), corticosterone (0.1 mg/mL in ddH₂O), and MK-571 sodium (0.1 mg/mL in ddH₂O), and N-Acetyl-L-cysteine (2 mg/mL in ddH₂O) were orally administered in drinking water for treated groups. Vehicle controls were orally administered in drinking water for control groups. 100 mg/kg Lipoic Acid (in DMSO) was orally administered per day during sleep deprivation by gavage at ZT0 for the antioxidant feeding group, and the vehicle control was orally administered at the equal volume for vehicle control group. 30 mg/kg Tariquidar (in 5% glucose and 4% DMSO) was *i.p.* injected 12 h prior to SD and 48 h after SD (the mice were kept in the cage with bedding and extra absorbent papers for 30 min to clean and dry their skin; and after the injection, the mice were kept in the same cage to recover for 1 h), and the vehicle was injected at the same time for the control group. 5 mg/kg Asapirant (in 50% DMSO) was orally administered twice by gavage at SD0h and SD12h, and the vehicle was also orally administered by gavage at equal volume for vehicle control group.

Blood glucose detection

For routine blood glucose examination in mice, blood glucose was determined at ZT0 through tail blood sampling with Accu-Chek Performa GlucoMeter (Roche). For oral glucose tolerance tests, mice were fasted 12 h before the test. The basal blood glucose was determined at ZT0, and then the mice were administered 2 g/kg glucose by oral gavage. After 15 min, 30 min, 60 min, and 120 min, blood glucose concentration determinations were repeated for individual mice.

Blood leukocyte separation

Each mouse was anesthetized with pentobarbital (*i.p.* injection 80 mg/kg) and 500 μ L of blood was taken retro-orbitally. Blood was collected in an EDTA anticoagulant tube (BD Biosciences). The blood sample was transferred into 5-fold volume of Ammonium-Chloride-Potassium (ACK) lysis buffer (150 mM NH₄Cl, 10mM KHCO₃, Na₂·EDTA 0.1nM, pH7.4), and incubated on ice (gently turn upside down 2 times during incubation) for 10 min. After 500 \times g centrifugation at 4°C for 10 min, the supernatant was completely discarded. The cell pellet was washed with 2-fold volume of ACK lysis buffer, and 500 \times g centrifuged at 4°C for 10 min.

Leukocyte bulk RNA sequencing

For blood sampling, each mouse was anesthetized with pentobarbital (*i.p.* 80 mg/kg) and 500 μ L of blood was taken retro-orbitally. Blood was collected in an EDTA anticoagulant tube (BD Biosciences). Total RNA was extracted from the blood samples of 3 mice in the same group with QIAamp RNA Blood Mini Kit (52304, Qiagen) following the manufacturer's instructions. Sequencing libraries were prepared with Illumina Truseq Library Prep Kits v2 (Illumina) according to the manufacturer's instructions. All libraries were guaranteed quality with quality check and sequenced by Illumina Hiseq X Ten platform with 300 bp paired-end reads at ~50M reads per samples. Low-quality raw data and adaptors were removed by Trimmomatic (v0.39).¹⁰⁸ STAR (v2.7.9a)¹⁰⁹ was used to align reads to the prebuilt mouse reference GRCm38/mm10. Uniquely mapped reads were assigned to genes based on the annotation file using FeatureCounts (v2.0.3)¹¹⁰ from Subread package and normalize expression levels for each sample to obtain Fragments Per Kilobase Million (FPKM). Heat maps showing gene expression data were generated using the ComplexHeatmap⁶³ package in R. RNA-seq data have been deposited for public access at the NCBI GEO database under accession number GSE213494.

Leukocyte single-cell RNA sequencing

For single-cell sequencing, leukocyte pellets of 3 mice in the same group were resuspended in equal amount with DPBS (containing 0.04% BSA), and the cell concentration was adjusted to 500–1,200 cells/ μ L. Each library was designed to contain around 7,000 cells, and sequencing depth was about 50,000 reads per cell. All libraries for single-cell RNA sequencing were prepared by Chromium Single Cell 3' Reagent Kits (v3 Chemistry, 10x Genomics) according to the manufacturer's instructions. Qualitative analysis of each DNA library was performed using an Agilent 2100 Bioanalyzer. The concentration of each DNA library was measured using a Qubit fluorometer (Invitrogen). Libraries were sequenced by Illumina Hiseq X Ten platform with 300 bp paired-end reads. Low-quality raw data and adaptors were removed by Trimmomatic (v0.39).¹⁰⁸ The filtered reads were processed with the standard Cellranger v4.0.0 pipeline (<https://support.10xgenomics.com/single-cell-gene-expression/software/overview/welcome>), and then mapped to the prebuilt mouse genome reference GRCm38/mm10. The barcode-feature matrixes generated by Cellranger were further analyzed with Seurat v3.0 pipeline¹¹¹ in R v4.0.2. In brief, the low-quality data (min.cells<3 and min.genes<200) and cells with more than 10% mitochondrial gene expression were filtered out. Seurat canonical correlation analysis (CCA) method was used for integrating the cells across

different conditions. Then, all cells were clustered using the top 50 dimensions of PCA and the resolutions were set to 0.8. Cell clusters were visualized using t-SNE plots, with all significant principal components as input. The cell type markers that conserved among different conditions were identified using the FindConservedMarkers function. Differential expression analysis among different groups within the specific cell cluster was performed by the FindMarkers function with MAST method. Cut-off of differential expression gene was set as \log_2 (Fold change) > 0.57 or < -0.57 and adj. p-value < 0.05. The gene ontology terms of differential expressed genes were performed using the web-based tool Enrichr.¹¹² scRNA-seq data have been deposited for public access at the NCBI GEO database under accession number GSE213496.

Detection of ROS in mouse small intestine

ROS was detected in mouse small intestines using Dihydroethidium (DHE, S6603, Bioyetime) as described with modifications.^{8,113} For tissue collection, mice were euthanized with overdose of pentobarbital (250 mg/kg), disinfected abdomen with 75% ethanol, and exposed the peritoneal cavity. About 1.5 cm of the small intestine after the duodenum was collected and placed in room temperature PBS. The intestine was cut open longitudinally using scissors and the fecal contents were removed. The small intestine was pinned to the dissection dish with the villi facing up in PBS; and the muscle layer was allowed to relax. Samples were washed 3 times before DHE staining. For DHE staining, samples were incubated for 30 min with 10 μ M DHE at 37°C in the dark. Samples were washed three times in PBS before embedding. For embedding and sectioning, the stained small intestine tissue was transferred to a pre-chilled OCT block with the villi facing up. The tissue was embedded in OCT and frozen on dry ice. Sections were cut at 25 μ m longitudinally. For imaging, the slides were washed in PBS for 30 seconds and mounted with 50% glycerol with DAPI. All procedures were completed within 6 hours. Then, the sections were imaged immediately with identical settings on a Zeiss LSM 800 using DAPI (blue) and Ethidium homodimer (red) channel. DHE relative intensity were calculated by the total intensity in the red channel dividing the area (particle analysis with the Huang's fuzzy thresholding method) in the blue channel using imageJ.

In vivo neutrophil depletion

Mice were *i.p.* injected with 20 mg/kg *InVivo*MAb anti-mouse Ly6G antibody (1A8 clone) once every 3 days, and control mice were *i.p.* injected with 20 mg/kg *InVivo*MAb rat IgG2a isotype control once every 3 days. The SD mice were injected twice during the SD procedure (12 h prior SD and 48 h after SD). Before the second injection, the mice were kept in the cage with bedding and extra absorbent papers for 30 min to clean and dry their skin; after the injection the mice were kept in the same cage to recover for 1 h before transforming to the SD condition. During this period, the mice were kept awake by gentle touch with feathers.

Neutrophil proportion detection

The separated blood leukocytes were washed with 500 μ L of flow cytometry staining buffer (eBioscience, 00-4222-26) and 500 \times g centrifuged at 4°C for 5 min. The leukocyte pellet was resuspended in flow cytometry stain buffer. For identifying neutrophils from leukocytes, the cells were stained with FITC anti-mouse CD45 (BioLegend, 30-F11), APC anti-mouse CD11b (BioLegend, M1/70), PE anti-mouse Ly6G (BioLegend, 1A8) for 30 min at 4°C in dark. The stained cells were washed twice with 1 mL of flow cytometry staining buffer and 500 \times g centrifuged at 4°C for 5 min. The leukocyte pellet was resuspended with 1 mL of flow cytometry stain buffer and filtered into the 5-mL polystyrene flow cytometry tube with 40 μ m cell strainer cap (Falcon, 720035). The blood leukocyte samples were analyzed with BD FACSAria III or BD FACSAria Fusion.

In vivo mononuclear phagocyte depletion

Mononuclear phagocytes were depleted by *i.p.* administration of clodronate liposomes (40337ES08, Yeasen). Briefly, 200 μ L of clodronate liposomes (in PBS) or vehicle were *i.p.* administrated every 3 days, and the first injection was performed 24 hours before SD began.

Depletion efficiency of mononuclear phagocytes was analyzed with flow cytometry as previous reported.^{114,115} In brief, 72 hours after *i.p.* administration of clodronate liposomes, mice were euthanized with an overdose of pentobarbital (250 mg/kg). For blood monocytes detection, blood leukocytes were collected as previously described. Cells were stained with FITC anti-mouse CD45 (BioLegend, 30-F11), APC anti-mouse CD115 (eBioscience, AFS98). For liver-resident macrophage detection, euthanized mice were disinfected with 75% ethanol. The peritoneal cavity was exposed and the liver was perfused with 10mL of PBS through the vena cava to the portal vein. The gallbladder was removed and the liver was cut into small pieces (1-2 mm³) and then transferred to a 50 mL Falcon tube containing 10 mL of pre-warmed digestion buffer (RPMI 1640 with 0.2 mg/mL of collagenase IV, 5 units/mL of DNase I, and 10% FBS). The sample was incubated at 37°C for 30 minutes and vortexed every 10 minutes. The digested liver was gently homogenized by pipetting and centrifuged at 50 \times g for 3 minutes to discard debris. The sample was then centrifuged at 400 \times g for 5 minutes to collect target cells. The erythrocytes were lysed with ACK lysis buffer and washed twice with flow cytometry staining buffer. Cells were stained with FITC anti-mouse CD45 (BioLegend, 30-F11), APC anti-mouse F4/80 (BioLegend, BM8). For the spleen-resident macrophages detection, the spleen was dissected and splenocytes were obtained by pressing through a 70- μ m cell strainer (352350, Falcon). After centrifugation at 500 \times g for 5 minutes at 4°C, the erythrocytes were lysed with ACK lysis buffer and washed twice with flow cytometry staining buffer. Cells were stained with FITC anti-mouse CD45 (BioLegend, 30-F11), APC anti-mouse F4/80 (BioLegend, BM8), PE anti-mouse Ly6G (BioLegend, 1A8). The staining and flow cytometry procedures were performed as previously described.

Serum extraction

For serum sampling, each mouse was anesthetized with pentobarbital (*i.p.* injection 80 mg/kg) and 600 μ L of blood was taken retro-orbitally. Blood was collected in a 1.5 mL Eppendorf tube. After 10-min coagulation at room temperature, the blood samples were 2,500 \times g centrifuged at 4°C for 10 min. The extracted serum was immediately used in assay or preserved at -80°C.

Serum cytokine & chemokine screen assay

Cytokines and chemokines in serum were determined with the U-PLEX Biomarker Group 1 (ms) 35-plex (Meso Scale Diagnostics, K15083K) or V-PLEX Proinflammatory Panel 1 Mouse Kit (Meso Scale Diagnostics, K15048D-X) following the manufacturer's instructions. Each kit contained 4 96-well plates to determine different biomarkers, and the serum samples were 1:2 diluted with dilution buffer for assay according to the preliminary test. For each SD group (SD12h, SD24h, SD48h), 5 sleep-deprived mice for respective time were included in assay. For the control group (SD0h), to diminish the circadian effect, 4 mice sampled at opposite phase (2 at ZT0 and 2 at ZT12) were included in assay. The concentrations of 8 cytokines or chemokines were below the least detectable level in more than half samples, and the concentrations of these cytokines or chemokines were only provided in Source Data.

ELISA

The concentration of serum corticosterone and IL-6 were determined by Corticosterone Parameter Assay Kit (R&D system, KGE009) and Mouse IL-6 Quantikine Elisa kit (R&D system, M6000B) respectively. Serum samples were obtained as above, and ELISA procedures were performed according to the manufacturer's instructions.

Chemical sympathectomy

Chemical sympathectomy was performed with 3 *i.p.* injections of 120mg/kg 6-hydroxydopamine hydrobromide (6-OHDA in DPBS solution). Injections were 72 h apart⁴⁸ with the last injection 16 h before SD. Mice injected 3 times with an equal volume of DPBS served as vehicle-treated control.

In vivo BBB efflux assay with rhodamine B

The procedure was adapted with modifications from a previous study.⁵⁷ In brief, mice were anesthetized with pentobarbital (*i.p.* 80 mg/kg), and then rhodamine B (RHB) (dissolved in saline, 5 mg/mL) was injected (10 mg/kg) into the jugular vein. After 90-min recovery, 250 μ L of blood was taken retro-orbitally, and serum was extracted as described above. Mice were then euthanized with an overdose of pentobarbital (*i.p.* 250mg/kg) and the remaining blood was removed through cardiac perfusion of PBS. The brains were harvested and homogenized in equal weight PBS with Dounce Tissue Grinder on ice. The brain homogenate supernatant was collected after 20-min 18,000 \times g centrifugation at 4°C. RHB fluorescence in the serum and homogenate supernatant was measured with EnSpire Multimode Plate Reader at Ex540nm/Em590nm. RHB concentration was determined by standard curve and the ratios of brain homogenate supernatant to serum were calculated for each mouse. The ratio of RHB concentration in brain over that in serum represents the BBB efflux efficiency through ABC in an inversely proportional relationship.

Mouse brain vessel purification

The procedure was adapted with modifications from a previous study.¹¹⁶ In brief, 3 mice were euthanized with an overdose of pentobarbital (*i.p.* 250mg/kg) and the remaining blood was removed through cardiac perfusion of PBS. The brains were dissected out the choroid plexus with tweezers under the stereomicroscope and chopped into small pieces of about 2 mm in 15 mL B1 solution (HBSS with 10 μ M HEPES). The brains were homogenized in B1 solution with a Dounce homogenizer via 20 strokes. The brain homogenate was transferred into a 50 mL tube and centrifuged at 2,000 g for 10 min at 4°C. The supernatant was discarded and the pellet was resuspended in 20 mL B2 solution (B1 with 30% Percoll) via vigorously shaking for 1 min. After centrifugation at 4,400 g for 15 min at 4°C, the upper myelin layer and the interlayer were carefully removed with the transfer pipette, and the tube was blotted with absorbent paper (avoid touching the vessel pellet). The vessel pellet was resuspended in 5 mL B3 solution (B1 with 1% BSA), and the suspended vessel was filtered with a pre-equilibrated 45 μ m-mesh filter followed by rinsing with 10 mL B3 solution. The mesh filter was removed with clean forceps and immediately immersed into a beaker with 20 mL B3 solution. The vessels were detached from the mesh filter by shaking. The content was transferred into a 50 mL tube and centrifuged at 2,000 g for 5 min at 4°C. The supernatant was removed and the vessel pellet was resuspended in 1 mL B1 solution, and transferred it into a 1.5 mL Eppendorf tube and kept on ice until further experiment.

Ex vivo ABC transport assay with rhodamine B

The procedure was adapted with modifications from a previous study.⁶⁰ In this assay, RHB exists in the incubation buffer and passively leaks into brain vascular endothelial cells. The active efflux of RHB is then mediated by ABC transporters, with remaining RHB in the endothelial cells indicating efficiency of ABC transporter-mediated efflux. Fresh mouse brain vessels were incubated at 37°C in B1 solution (HBSS with 10 μ M HEPES) containing 5 μ M RHB for 60 min. Centrifuge at 2,000 g for 10 min at 4°C, discard the supernatant, and the pellet was resuspended in 1 mL B1 solution. The pellet was washed for 3 times with the same procedure. Then, the vessel pellet was resuspended in the blocking solution (B1 with 5% BSA), and incubated 60 min at room temperature with gently shaking. Replace the blocking solution with the mixture of anti-mouse CD31 antibody (BD Biosciences, MEC 13.3, 1:200 dilution) and

the blocking solution, and incubate at room temperature for 2 hours. After 3 washes with the blocking solution, incubate the mixture of the goat anti-rat IgG (Alexa Fluor® 488) antibody (1:1000 dilution) and the blocking solution for 2 hours at room temperature. After 3 washes with B1 solution, resuspend the vessel pellet with 50 μ L of B1 solution and add 50 μ L mounting solution (50% DPBS, 50% glycerin, and 0.5 μ g/mL DAPI). Transfer the vessels to a glass slide and cover with a coverslip. Vessels are observed under a confocal microscope (Zeiss LSM 800). Distinguish the vessels with DAPI staining and snap photos under DAPI, Alexa 488, and RHB channels. Alexa 488 channel is used to show the cross-sectional area of the vessel, and RHB channel is used to show the total Rhodamine B transported through ABCB1 into inside of the vessel. The images were analyzed with ImageJ, and the RHB integrated density over the cross-sectional area represents the ABC transport efficiency of the mouse brain vessels in a direct proportional relationship.

PGD₂ Brain Efflux Index (BEI) Assay

The procedure was adapted with modifications from the previous study.^{84,85,117} The BEI was defined as the relative percentage of the drug or metabolite effluxed from the cerebrum to the peripheral across the BBB compared to the amount of the drug or metabolite injected into the cerebrum, with the following formula:

$$100 - \text{BEI}(\%) = \frac{\text{amount of molecule retained in cerebrum}}{\text{amount of impermeable reference retained in cerebrum}} \times \frac{\text{amount of impermeable reference injected into cerebrum}}{\text{amount of molecule injected into cerebrum}} \times 100$$

Inulin worked as the impermeable reference, thus, the PGD₂ BEI value of mouse was calculated with the following formula:

$$100 - \text{BEI}(\%) = \frac{[{}^3\text{H}]\text{PGD}_2\text{retained in cerebrum}}{[{}^{14}\text{C}]\text{Inulinretained in cerebrum}} \times \frac{[{}^{14}\text{C}]\text{Inulin injected into cerebrum}}{[{}^3\text{H}]\text{PGD}_2\text{injected into cerebrum}} \times 100$$

The intracerebral microinjection was performed as described.^{84,117} In brief, 8-week mice were anesthetized with pentobarbital (*i.p.*, 80 mg/kg). 0.005 μ Ci/ μ L [¹⁴C]Inulin (American Radiolabeled Chemicals, ARC0124) and 0.1 μ Ci/ μ L [³H]PGD₂ (PerkinElmer, NET616100UC) were dissolved in ECF buffer (122mM NaCl, 25mM NaHCO₃, 10 mM D-glucose, 10 mM HEPES, 3 mM KCl, 1.4mM CaCl₂, 1.2 mM MgSO₄; pH7.4). 1 μ L of the injectate was microinjected into the secondary somatosensory cortex (S2) region (AP -1.2 mm; ML +3.0 mm; 2.8 mm from skull) and the needle left in the injection configuration for an additional 4 min before being slowly retracted. After the designated time (5 min, 20 min, and 40 min), the mouse was decapitated and the ipsilateral cerebrum was separated and dissolved in 2 mL 2 M NaOH at 55°C for 3 h. Then, the homogenate was mixed with 14 mL of Ultima Gold XR liquid scintillation cocktail (PerkinElmer, 6013119), and ³H- and ¹⁴C-derived radioactivity was measured by a Tri-Carb 3810TR liquid scintillation counter (PerkinElmer). (100-BEI) (%) of 5-min samples in each group were regarded as 100.

GRAB_{PGD2} Development

To develop a PGD₂ sensor, a cpGFP module from GRAB_{NE1m} with flanking peptide linkers¹¹⁸ was firstly inserted into human DP1 receptor for preliminary experiments, and subsequently swapped into bat DP1 receptor. All sensor variants plasmids were generated by Gibson assembly and subcloned into the pDisplay expression vector. DNA fragments were generated using PCR amplification with primers with ~25 bp overlap, and all sequences were verified using Sanger sequencing. The plasmids used to express the GRAB_{PGD2} sensor in HEK293T cells were based on the pDisplay vector: a IgK secretion signal peptide was added to the N terminal of GRAB_{PGD2} sensors, following an IRES-mCherry-CAAX to ensure labeling the cell membrane with mCherry. The Gibson assembly product was then transformed into DH5 α competent cells and the E. coli was allowed to grow for 12-16 h to form visible colonies. Then the colonies were picked into a 96-well plate with 1.2 mL LB+ medium with ampicillin. The E. coli was cultured for additional 12-16 h in a 37°C shaker with 220 rpm. Then the plasmid was purified with a 96-well extraction column.

Fluorescence imaging of HEK293T cells expressing GRAB_{PGD2}

HEK293T cells were plated on 96-well plates and cultured at 37°C, 5% CO₂ in DMEM (Gibco) supplemented with 10% (v/v) fetal bovine serum (Gibco) and 1% penicillin-streptomycin (Gibco). At 60-70% confluency, cells were transfected with GRAB_{PGD2} plasmids using PEI MAX® (Polyscience, 24765-100) (~200 ng DNA/well for 96-well plates, PEI:DNA = 3:1) for 6 h and then were changed to fresh culture medium. Imaging was performed 36 h after transfection. The culture medium was replaced before imaging with Tyrode's solution (150 mM NaCl, 4 mM KCl, 2 mM MgCl₂, 2 mM CaCl₂, 10 mM HEPES, and 10 mM glucose, pH 7.4).

HEK293T cells in 96-well plates were imaged using an Opera Phenix high-content screening system (PerkinElmer) equipped with a 20x/0.4 NA objective water-immersion objective, a 488 nm laser and a 561 nm laser. Green and red fluorescence were respectively collected using a 525/50-nm emission filter and a 600/30-nm emission filter. The fluorescence intensity changes of the GRAB_{PGD2}

was calculated using the GFP/mCherry ratio change. PGD₂ were diluted with Tyrode's solution at the indicated concentrations. Imaging experiments were performed at room temperature (22–24°C).

As for the dose response curve measurement for PGD₂ and brain homogenates, PGD₂ and brain homogenates were diluted with Tyrode's solution, and HEK293T cells expression GRAB_{PGD2-1.0} were used.

Confocal imaging of cultured neurons expressing GRAB_{PGD2-1.0}

The rat cortical neurons were isolated from postnatal day 0 (P0) Sprague-Dawley rat pups. Briefly, the brains were removed and the whole cortex was dissected. Further digested with 0.25% trypsin-EDTA (Gibco), the supernatant was collected and then centrifuged with 800 rpm, 5 min. After discard the supernatant, the pellet was resuspended and cells were subsequently plated on poly-D-lysine (Sigma-Aldrich) coated 12-mm glass coverslip. The neurons were cultured in neurobasal medium (Gibco) supplemented with 2% B-27 (Gibco), 1% GlutaMax (Gibco), and 1% penicillin-streptomycin (Gibco) at 37°C with 5% CO₂.

The plasmids used to express the GRAB_{PGD2-1.0} sensor in rat cortical neurons were cloned into the pAAV vector under the control of human synapsin promoter (hSyn) promoter. The AAV2/9-hSyn-GRAB_{PGD2-1.0} virus was prepared by Shandong Vigene Biosciences with viral titer higher than 1×10¹³. After cultured for 6 days in vitro, the rat cortical neurons were infected with ~5×10¹² AAV2/9-hSyn-GRAB_{PGD2-1.0}. Before imaging, the neurons were cultured for additional 7–9 days to allow sensor expression.

Rat cortical neurons growing on 12-mm coverslips were imaged using a Ti-E A1 confocal microscope (Nikon) equipped with a 10x/0.45 NA objective, a 20x/0.75 NA objective, a 40x/1.35 NA oil-immersion objective, a 488-nm laser, and a 561-nm laser; green and red fluorescence were recorded using 525/50-nm and 595/50-nm emission filter respectively. The fluorescence intensity changes of the GRAB_{PGD2-1.0} was calculated using the GFP/mCherry ratio change. PGD₂ and brain homogenates were diluted with Tyrode's solution at the indicated concentrations. Imaging experiments were performed at room temperature (22–24°C).

Fiber photometry recording and analysis of GRAB_{PGD2-1.1}

For AAV virus injection and fiber implantation, each 7- to 8- week-old mouse was anesthetized with pentobarbital (*i.p.* 80 mg/kg). The skull was exposed and then cleaned using cotton swabs soaked in 5% hydrogen peroxide. Stereotaxic injection of 500 nL of AAV9-EF1 α -GRAB_{PGD2-1.1} into the POA (AP 0 mm; ML +0.65 mm; DV 5 mm) was performed at a rate of 50 nL/min via a glass pipette micro-injector, followed by implantation of an optical fiber cannula (200 μ m, NA=0.37) positioned at a distance of 0.1 mm above the virus injection site and secured with dental cement. Experiments were conducted at least 2 weeks after surgery.

GRAB_{PGD2-1.1} fluorescence was recorded using Inper Multi-Channnel Fiber Photometry Device with excitation channels set to wavelengths of both 410 nm and 470 nm. The excitation light power at the top of the optical fiber was adjusted to 20–30 μ W and delivered at 20 Hz with 10 ms pulse duration for 5 s every 5 min. In order to minimize autofluorescence from the optical fiber, the recording fiber was pre-photobleached using a high-power light source.

After a minimum of 2 days of habituation to the recording environment, the mice were connected to the device via an optical fiber for baseline recording lasting 3 hours. Subsequently, they were transferred to a new context (another Con environment) and recorded for more than 12 hours. At the same time point on the second day, baseline recording on the same mouse was conducted for 3 hours before subjecting to SD and continuing with SD recording for more than 12 hours.

The photometry data were analyzed using Inper Data Analysis software with Delete Interval function (Retained Duration set at 3s, no Baseline Correction) applied to remove redundancy in both channels. Background autofluorescence and baseline correction were processed using default settings (Polyfit, Poly Order=2). The calculated GRAB_{PGD2-1.1} fluorescence was averaged every 3 seconds as representative of each recording duration. F₀ was defined as average fluorescence during the two-hour period prior to Con or SD recordings, and $\Delta F/F_0$ and z-score transformed $\Delta F/F_0$ time-series were computed accordingly. Finally, peak z-score transformed $\Delta F/F_0$ during SD recording was used as normalization factor for time-series z-score transformed $\Delta F/F_0$ in both Con and SD recordings.

Tetranor-PGDM concentration measurement

The LC-MS analysis of tetranor-PGDM was performed using a published method⁸¹ with slight modifications. A stock solution of tetranor-PGDM at 2.5 mg/mL was used to prepare working standard solutions of 0.5, 1, 2, 5, 10, 20, 50, 100 ng/mL by serial dilution in methanol: H₂O (1:1). 100 μ L of mouse serum or standard solution was added to 50 μ L of aqueous solution of methoxyamine hydrochloride (1 g/mL) and allowed to stand for 15 min at room temperature. The samples were purified by solid phase extraction (SPE) using StrataX C18 8B-S100-UAK cartridges (Phenomenex, 8B-S100-UAK). After pre-conditioning with 1 mL of acetonitrile and 1 mL water, the SPE cartridge was loaded with the sample and washed with 1 mL of 5% acetonitrile in water. Tetranor-PGDM was then eluted with 1 mL of 5% acetonitrile in ethyl acetate. The eluate was dried by vacuum concentrator and resuspended with 100 μ L of 5% acetonitrile in water for analysis.

LC-MS analysis was performed on a Thermo Vanquish UHPLC equipped with a Thermo Q Exactive HF-X hybrid quadrupole-Orbitrap mass spectrometer. A Waters Acquity UPLC CSH C18 column (1.7 μ m, 2.1 × 100 mm) was used for separation. The mobile phases consisted of 0.005% acetic acid in water adjusted to pH5.7 with ammonium hydroxide (A) and acetonitrile (B). The following gradient was applied: 0–1 min, 5% B; 1–5 min, 5–95% B; 5–7 min, 95% B; 7–7.01 min, 95–5% B; 7.01–10 min, 5% B. The flow rate was 0.4 mL/min and the column temperature was 35°C. The injection volume was 6 μ L.

Full-scan mass spectra were acquired in the range of m/z 100 to 1200 in negative ESI mode with the following source settings: spray voltage: 2.5 kV, auxiliary gas heater temperature: 380 °C, capillary temperature: 320 °C, sheath gas flow rate: 30 units, and auxiliary gas flow: 10 units. MS1 scan parameters included resolution 60000, AGC target 3e6, and maximum injection time 200 ms. Data processing was performed with Thermo Xcalibur software (4.2). Tetranor-PGDM [M-H]⁻ (m/z 385.198) was used for quantitation.

Adult brain chimeric-KO rAAV construction

AAV-based adult brain chimeric-KO platform were built based on a previous study.⁸⁶ Briefly, adult brain chimeric-KO of *Ptgds* by triple-target CRISPR/Cas9. *Ptgds* and non-target (NT) control were designed based on the Mouse GeCKO v2 Library.¹⁰⁵ Oligonucleotides for individual sgRNAs were inserted into pAAV-U6-sgRNA-hSyn-Cre-2A-EGFP-KASH-WPRE (60229, Addgene) to construct pAAV-3xsgRNA^{Ptgds} and pAAV-3xsgRNA^{NT}. Then, rAAVs were packaged, purified were performed by NIBS Genetic Screening Center following the previous study.

Retro-orbital rAAV injection

For adult brain chimeric-KO of *Ptgds* and NT, the mice were anesthetized with pentobarbital (i.p. 80 mg/kg) and administered with 10^{12} vg/mouse by retro-orbital injection. Experiments were more than two weeks after rAAV injection for stable expression of sgRNA across the mouse brains.

Brain lysate preparation and immunoblotting

The mouse brains were quickly dissected and lysed in cold RIPA lysis buffer (P0013B, Beyotime) supplemented with M5 Protease Inhibitor Cocktail (MF182, Mei5bio) using Dounce Tissue Grinder on ice for 10 min. After 20,000 g centrifugation for 20 min, the supernatant was transferred into a new tube and stored at -80°C. The brain lysate was mixed with SDS-PAGE Sample Loading Buffer (P0015F, Beyotime) and boiled at 105°C for 10 min.

Immunoblotting was performed with a standard protocol with following antibodies: anti-beta Actin antibody (1:80,000, 66009, Proteintech), anti-Prostaglandin D Synthase (Lipocalin)/PDS antibody (1:750, ab182141, Abcam), anti-rabbit IgG HRP-linked antibody (1:1,000, 7074, CST), and anti-mouse IgG HRP-linked antibody (1:5,000, 7076, CST).

DP1 and DP2 agonist administration

The mice were *i.v.* injected with 4 mg/kg Treprostinil (DP1 agonist, in 30% DMSO and 70% DPBS (v/v)), 4 mg/kg L888607 (DP2 agonist, in 30% DMSO and 70% DPBS (v/v)), or the combination of 4 mg/kg Treprostinil and L888607. Control mice were *i.v.* injected with vehicle. Then, blood leukocytes were sampled 16 h after injection. For dose-dependent DP1 agonist neutrophilia assay, 1 mg/kg, 2 mg/kg, and 4 mg/kg Treprostinil were used.

Cecal ligation and puncture (CLP) model

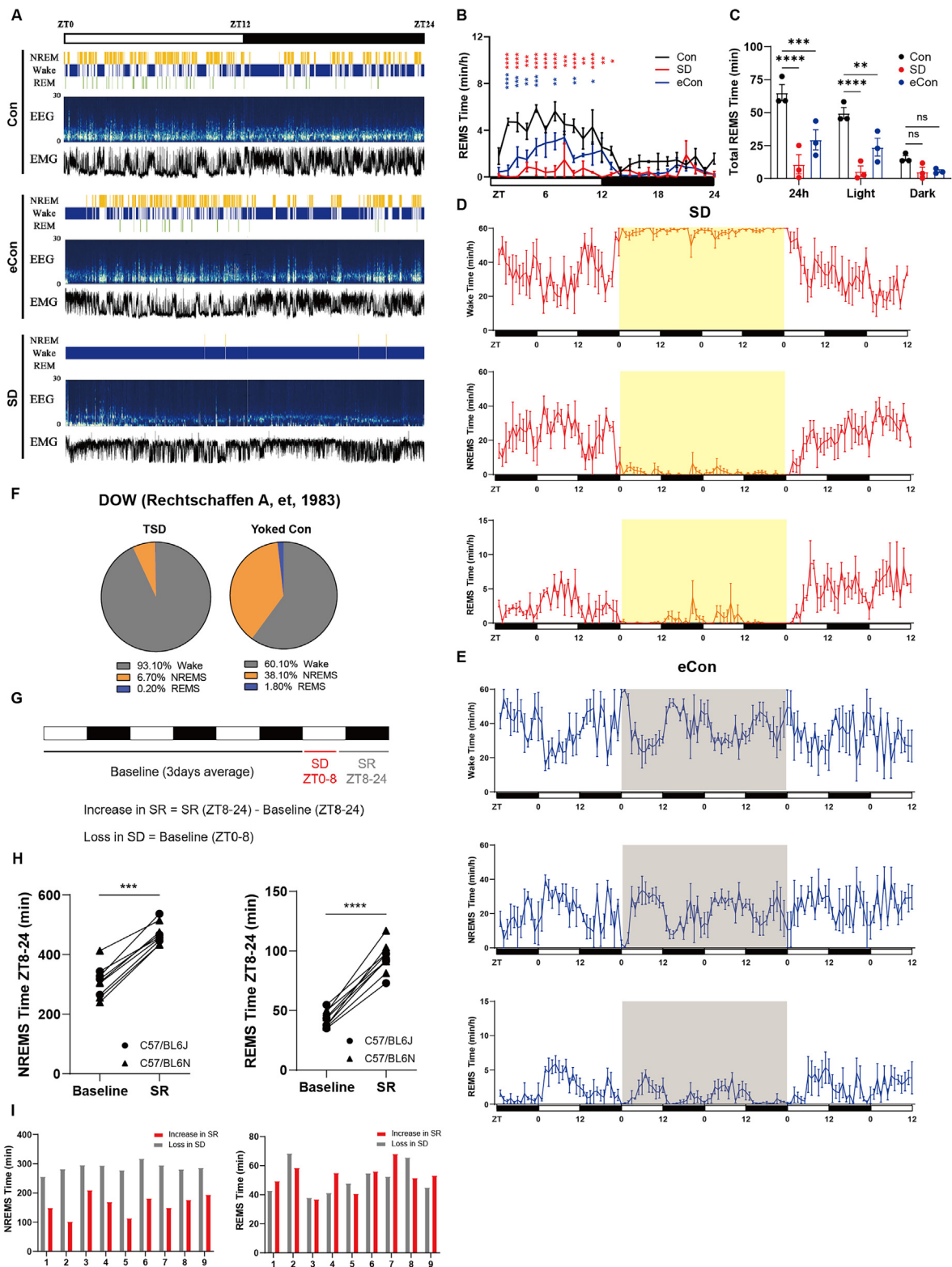
The CLP model procedure was adapted from previous methods.^{88,89} Briefly, carefully make a 1.5 cm longitudinal skin and peritoneum incision on the anesthetized mouse. Then isolate and exteriorize the cecum with forceps. Ligate 60% of the cecum to induce between mid- to high-grade sepsis according to the method.⁸⁸ Push the cecal contents towards the distal cecum, and perforate the cecum by single through-and through puncture in mesenteric-to-antimesenteric direction with a 21G needle. Ensure the patency by pushing a small droplet of feces from the penetration holes. Relocate the cecum into the abdominal cavity, then close the peritoneum and skin by running sutures. At last, resuscitate the mice by subcutaneous injection of 37°C saline.

The oral administration of 2.5 mg/kg Asapiprant (in 50% DMSO) was performed once every day by gavage, and equal volume of vehicle was oral administrated. The oral administration of MK-571 was performed by adding MK-571 sodium salt (0.1 mg/mL) into the drinking water. The oral administration of Asapiprant and MK-571 began 24 h prior the CLP procedure.

QUANTIFICATION AND STATISTICAL ANALYSIS

All data were presented as means \pm SEM unless otherwise indicated, and the statistical analysis performed were indicated in the figure legend. Statistical comparisons were analyzed in GraphPad Prism 9 (GraphPad Software) with two-way ANOVA test with multiple comparison (for comparisons of the influence of two different categorial independent variables, e.g., ZT and SD), one-way ANOVA test with multiple comparison (for comparisons among more than two groups with one variable), the Student's t-test (for comparisons between two groups), Mann-Whitney U test (for comparisons between two independent groups), or the log-rank test (for comparisons of survival curves). All data were subjected to the Grubb's test to guarantee the absence of outlier data points. Figures were prepared with GraphPad Prism 9 or R v4.0.2.

Supplemental figures



(legend on next page)

Figure S1. Curling prevention by water paradigm efficiently induces prolonged sleep deprivation in mice, related to Figure 1

(A) Representative 24-h EEG/EMG recordings of SD, eCon, and Con mice with sleep stage labels.

(B and C) Hourly plot of REMS time (B) and quantification of total REMS time (C) of adult mice ($n = 3$) subjected to SD, eCon, or Con.

(D and E) Hourly plot of wake, NREMS, and REMS time for mice ($n = 3$ per group) subjected to SD (D) or eCon (E) for 48 h with 36 h prior and 36 h after treatment (under Con).

(F) The amount of wake, NREMS, and REMS over 24 h for rats under total sleep deprivation (TSD) or the yoked controls ($n = 8$ per group) in the DOW paradigm (data adapted from Rechtschaffen et al.¹¹).

(G) Experimental schematic of sleep recovery recording after SD.

(H) Individual ZT8–ZT24 amounts of NREMS (left) or REMS (right) during baseline and SR.

(I) Individual amount of NREMS (left) or REMS (right) rebound during SR and loss during SD.

Data are presented as means \pm SEM. Statistical analysis was performed using two-way ANOVA with Dunnett correction test (B and C), two-way ANOVA with Sidák correction test (H). ns, not significant; * $p < 0.05$; ** $p < 0.01$; *** $p < 0.001$; **** $p < 0.0001$.

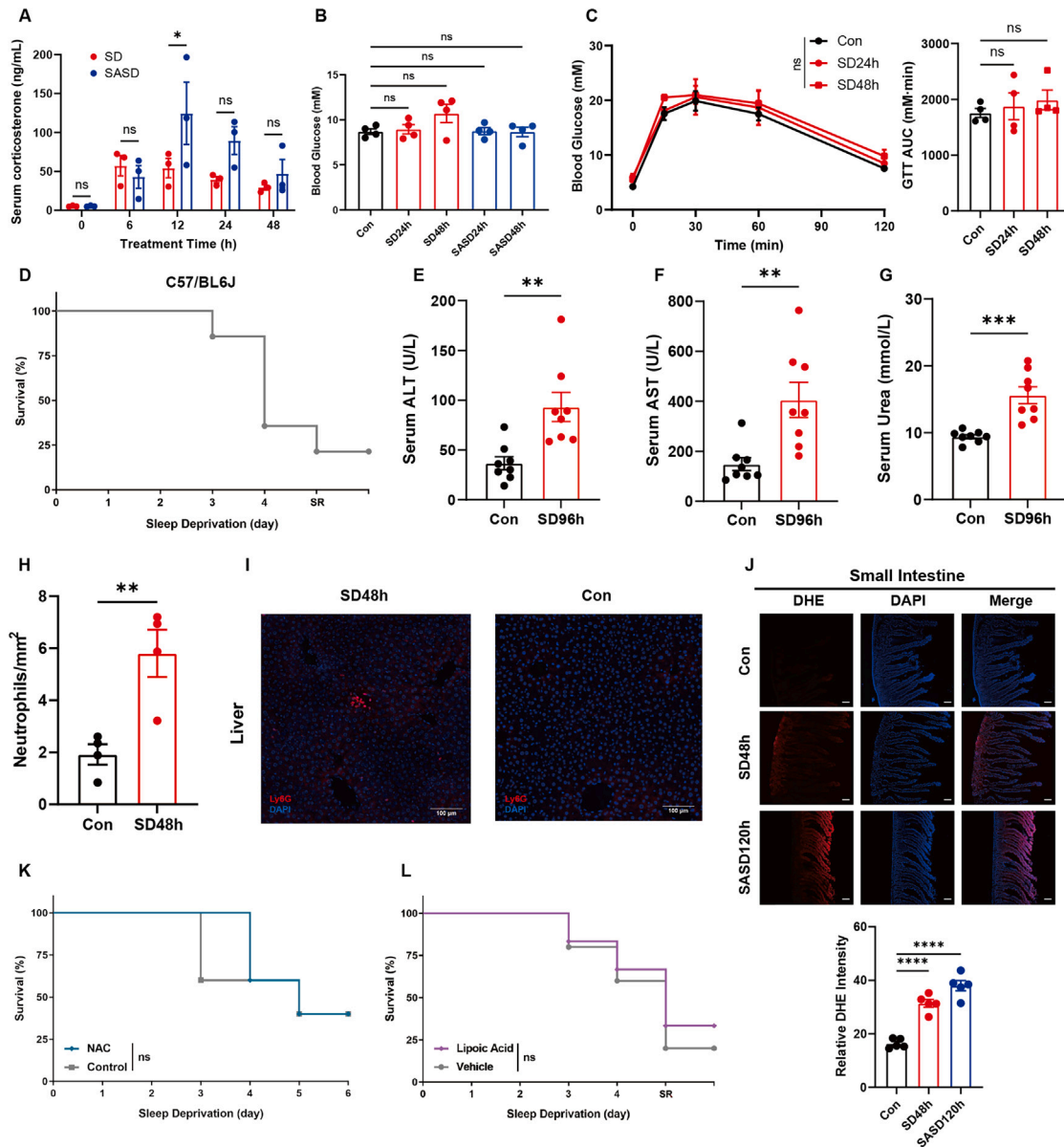


Figure S2. Physiological and pathological examinations of mice after sleep deprivation, related to Figures 1 and 2

(A) Serum corticosterone concentrations of mice ($n = 3$ per group) after indicated times of SD and SASD.
 (B) ZT0 blood glucose concentrations of mice ($n = 4$ per group) under Con, SD24h, SD48h, SASD24h, and SASD48h at ZT0.
 (C) Blood glucose concentrations during glucose tolerance test (GTT) and corresponding area under the curve (AUC) during GTT of mice ($n = 4$ per group) under SD24h, SD48h, and Con.
 (D) Detailed survival curve for C57BL/6J mice ($n = 14$) subjected to SD (SR means 48 h of recovery after SD).
 (E–G) Serum ALT (E), AST (F), and urea (G) concentrations of SD96h and Con mice ($n = 8$ per group).
 (H) Neutrophil infiltration intensities in livers of SD48h and Con mice.
 (I) Representative fluorescence microscopy images showing fluorescence of Ly6G (red) and DAPI (blue) in the liver sections of SD48h and Con mice.
 (J) Representative confocal images (upper) and relative dihydroethidium (DHE) intensities (lower) showing DHE fluorescence (red) in small intestine sections from C57BL/6J mice ($n = 5$) under SD48h, SASD120h, or Con. Scale bars, 100 μm .
 (K) Survival curves of mice subjected to SD (SR means 48 h of recovery after SD) with oral administration of NAC ($n = 5$) in the drinking water compared with controls ($n = 5$).
 (L) Survival curves of mice under SD (SR means 48 h of recovery after SD) with oral administration of liponic acid ($n = 6$) or vehicle ($n = 5$) by gavage.
 Data are presented as means \pm SEM. Statistical analysis was performed using two-way ANOVA with Sidak correction test (A), one-way ANOVA with Dunnett correction test (B, C, right, and J, lower), two-way ANOVA with Turkey correction test (C, left), two-tailed unpaired t test (E–H), or log-rank test (K and L). ns, not significant; ** $p < 0.01$; *** $p < 0.001$; **** $p < 0.0001$.

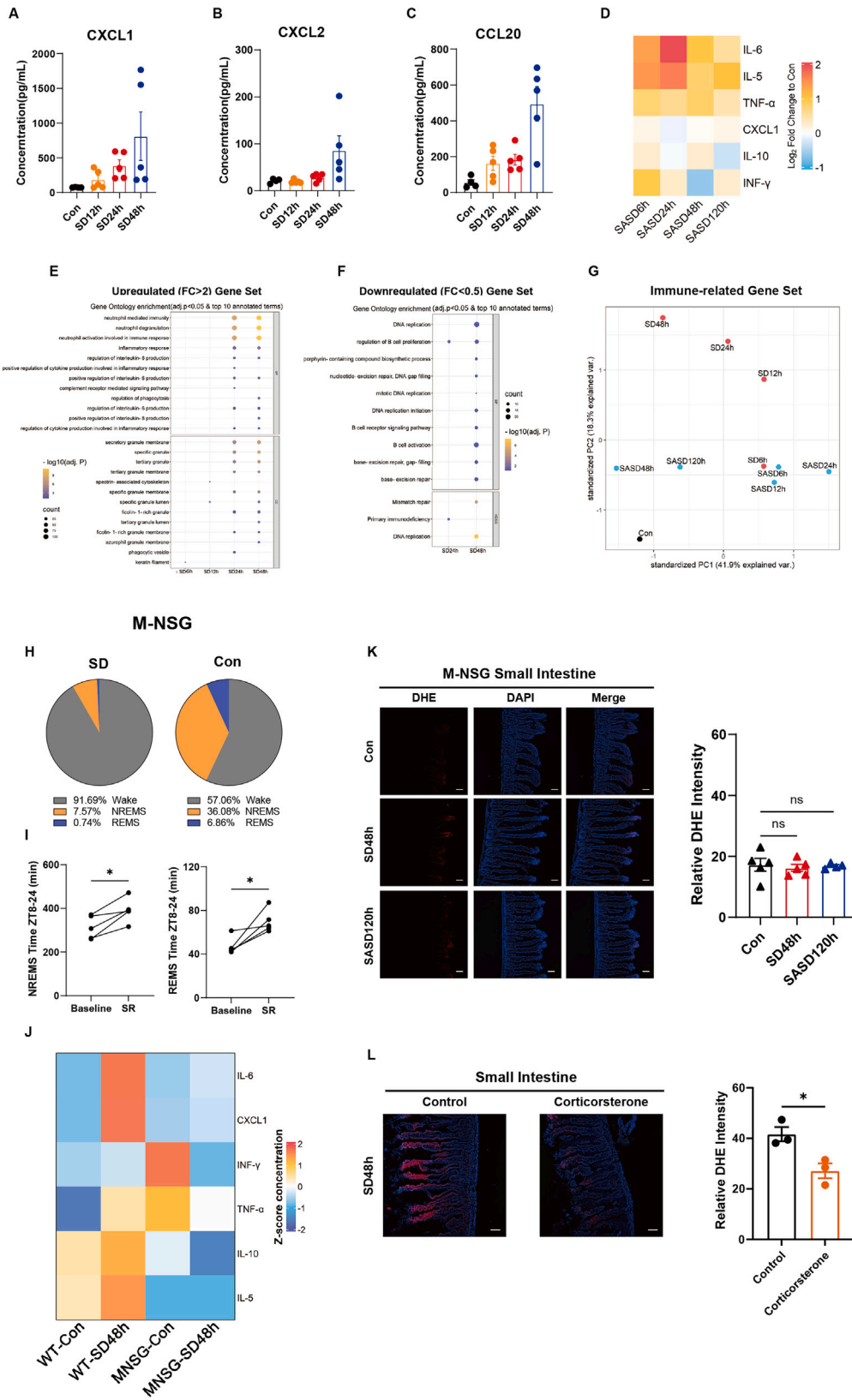


Figure S3. Sleep deprivation induces the accumulation of proinflammatory factors, related to Figure 2

(A–C) Serum CXCL1 (A), CXCL2 (B), and CCL20 (C) concentrations (n = 4 or 5 per group) of SD12h, SD24h, SD48h, and Con mice.

(D) The fold changes of serum cytokine and chemokine levels in mice subjected to SASD (n = 4) compared with Con after the indicated times.

(E) GO analysis of genes upregulated (FC > 2) in blood leukocytes of SD6h, SD12h, SD24h, and SD48h mice in the term of BP and CC categories.

(F) GO analysis and Kyoto encyclopedia of genes and genomes (KEGG) analysis of genes downregulated (FC < 0.5) in blood leukocytes of SD6h, SD12h, SD24h, and SD48h mice; no significant terms in SD6h and SD12h.

(G) PCA plots based on the FPKM of immune-related gene sets in blood leukocytes for mice subjected to different amounts of SD or SASD.

(H) The amount of total wake, NREMS, and REMS time over 24 h for M-NSG mice (n = 3) under SD or Con (for baseline sleep/weak recording).

(I) Individual ZT8–ZT24 NREMS (left) or REMS (right) amounts during baseline and SR in M-NSG mice (n = 4).

(J) Z score normalized serum concentrations of cytokines and chemokines in M-NSG and WT mice (n = 4) under SD48h or Con.

(K) Representative confocal images (left) and relative DHE intensities (right) showing DHE fluorescence (red) in small intestine sections from M-NSG mice (n = 4 or 5) subjected to SD48h, SASD120h, or Con. Scale bars, 100 μ m.

(L) Representative confocal images (left) and relative DHE intensities (right) showing DHE fluorescence (red) in small intestine sections of SD48h mice (n = 3) treated with corticosterone in the drinking water or controls. Scale bars, 100 μ m.

Data are presented as means \pm SEM. Statistical analysis was performed using one-way unpaired two-tailed t test (I and L, right) or ANOVA with Dunnett correction test (K, right). ns, not significant; *p < 0.05.

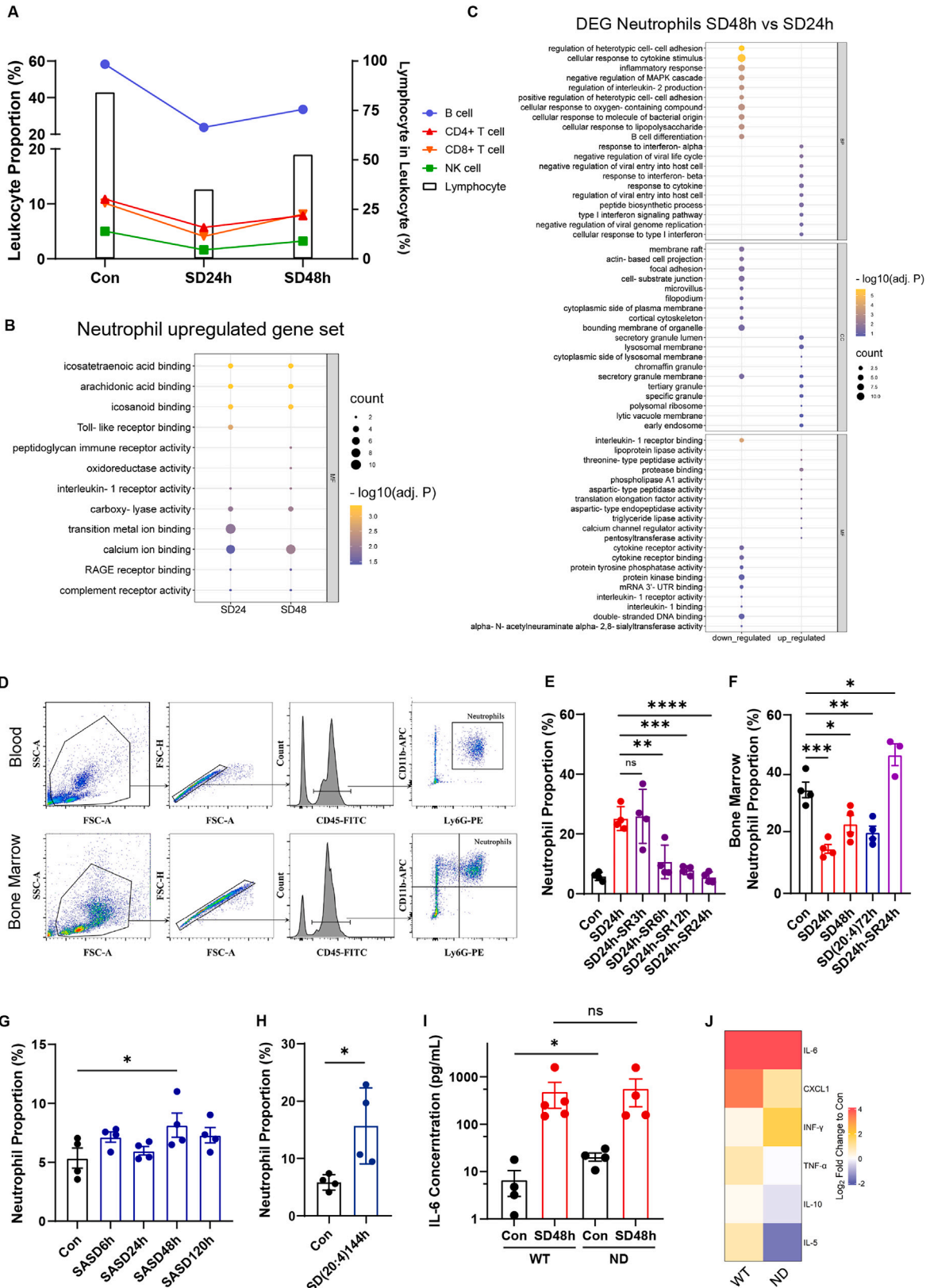


Figure S4. The accumulation and activation of circulating neutrophils during sleep deprivation, related to Figure 3

(A) The proportions of B cells, CD4⁺ T cells, CD8⁺ T cells, NK cells, and total lymphocytes in blood leukocytes of Con, SD24h, and SD48h mice according to scRNA-seq analysis. Left y axis indicates individual lymphocyte proportion (points) in blood leukocytes, right y axis indicates the total lymphocyte proportion (bar) in blood leukocytes.

(B and C) Gene ontology analysis of neutrophil DEGs of SD24h and SD48h over Con (B) or SD48h over SD24h (C). Top-10 ranking GO BP, CC, and molecular function (MF) terms with adjusted; $p < 0.05$ are shown.

(D) Gating strategy for neutrophils (CD45⁺CD11b⁺Ly6G⁺) in blood (upper) and bone marrow (lower).

(E) The proportion of neutrophils among blood CD45⁺ leukocytes in mice ($n = 4$) subjected to SD24h followed by SR3h, SR6h, SR12h, or SR24h.

(F) The proportion of neutrophils among bone marrow CD45⁺ leukocytes in mice ($n = 3$ or 4) under Con, SD24h, SD48h, SD(20:4)72h, or SD24h-SR24h.

(G) The proportion of neutrophil among blood CD45⁺ leukocytes in SASD-subjected mice ($n = 4$) after the indicated times.

(H) The proportion of neutrophils among blood CD45⁺ leukocytes in mice ($n = 4$) under SD(20:4) for 144 h.

(I) Serum IL-6 concentrations in ND and WT mice ($n = 4$ each) of Con or SD48h groups.

(J) The fold changes of serum cytokines and chemokines in ND and WT mice ($n = 4$) after SD48h compared with Con.

Data are presented as means \pm SEM. Statistical analysis was performed one-way ANOVA with Dunnett correction test (E–G) or two-tailed unpaired t test (H and I). ns, not significant, * $p < 0.05$; ** $p < 0.01$; *** $p < 0.001$; **** $p < 0.0001$.

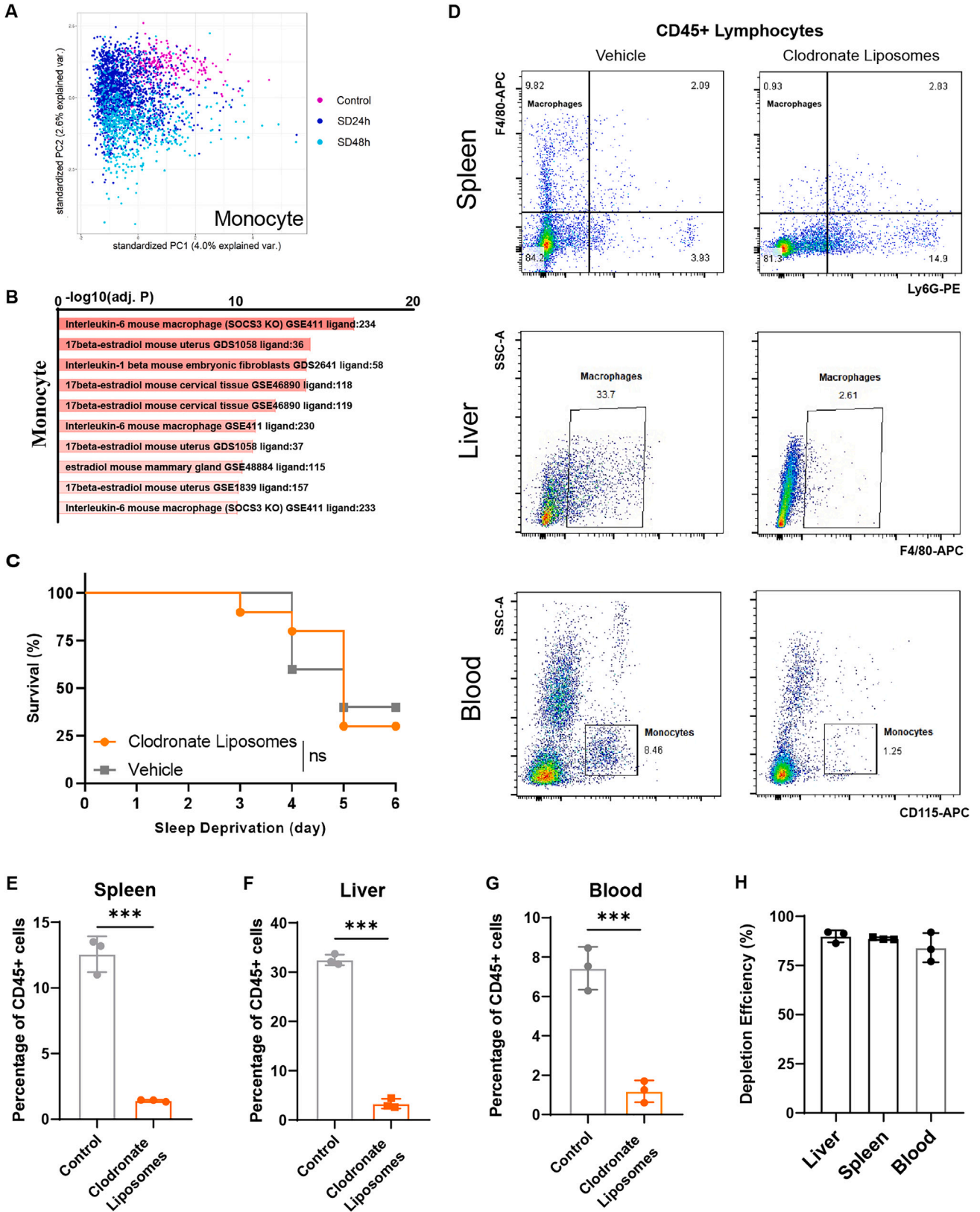


Figure S5. Characterization of the role of mononuclear phagocytes in sleep deprivation, related to Figure 3

(A) PCA plots showing individual monocytes in SD24h, SD48h, and Con mice.

(B) Bar chart of genes upregulated by SD in monocyte enrichment analyses in Enrichr using Ligand_Perturbations_from_GEO_up gene set.

(C) Survival curves of mice under SD (SR means 48 h of recovery after SD) with i.p. administration of clodronate liposomes (n = 10) or vehicle controls (n = 5).

(D) Gating strategy for macrophages in spleen (CD45+F4/80+Ly6G⁻, upper), liver (CD45+F4/80+, middle), and monocytes in blood (CD45+CD115+, lower).

(E–G) The proportion of mononuclear phagocytes among CD45⁺ leukocytes in spleen (E), liver (F), and blood (G) 24 h after i.p. administration of clodronate liposomes (n = 3) or saline (n = 3).

(H) The efficiency of mononuclear phagocyte depletion in liver, spleen, and blood by i.p. administration of clodronate liposomes (n = 3).

Data are presented as means ± SEM. Statistical analysis was performed using log-rank test (C) or two-tailed unpaired t test (E–G). ns, not significant; ***p < 0.001.

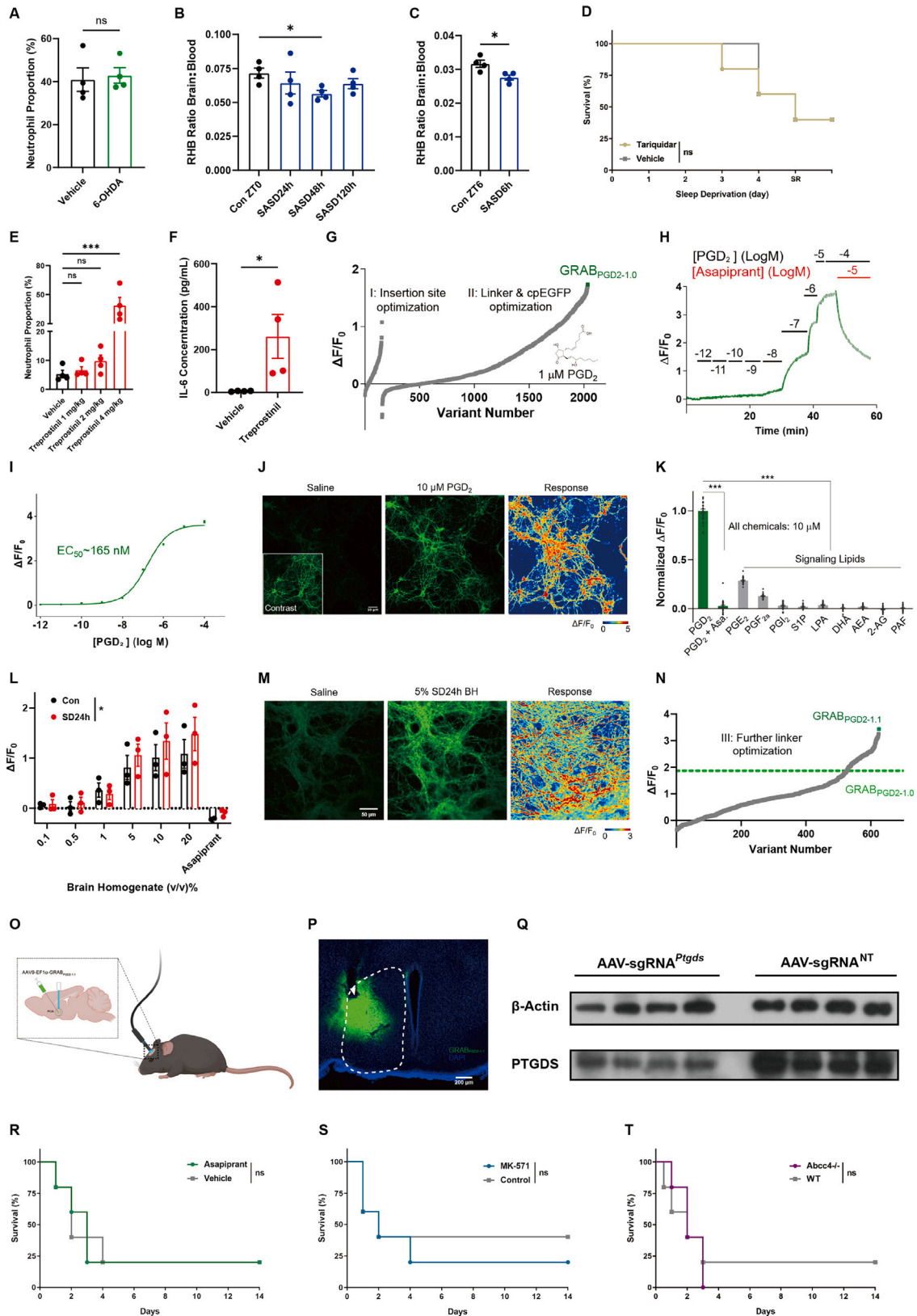


Figure S6. Sleep deprivation induces both enhanced BBB efflux and increased levels of PGD₂ in the brain, related to Figures 4, 5, and 6

- (A) The proportion of neutrophils among blood CD45+ leukocytes in chemically sympathectomized mice (n = 4, via i.p. injection of 6-OHDA) or vehicle controls (n = 4) under SD24h.
- (B and C) RHB brain homogenate over serum concentration ratios in mice (n = 4) after the indicated time under SASD (B for 24, 48, and 120 h; C for 6 h), compared with controls.
- (D) Survival curves of mice under SD (SR means 48 h of recovery after SD) with i.p. administration of tariquidar (n = 5) or vehicle (n = 5).
- (E) The proportion of neutrophils among blood CD45+ leukocytes in mice (n = 3 or 4) 16 h after i.v. administration of 1, 2, or 4 mg/kg of treprostinil, or vehicle.
- (F) IL-6 serum concentrations of mice (n = 4) 16 h after i.v. administration of 4 mg/kg treprostinil or vehicle.
- (G) Optimization steps for GRAB_{PGD2-1.0} and fluorescence responses to 1 μM PGD₂.
- (H) Representative trace of fluorescence responses measured in a GRAB_{PGD2-1.0} expressing neuron with the indicated concentrations of PGD₂ (black) and followed by the addition of 10 μM asapirant (red).
- (I) The dose-response curve measured in GRAB_{PGD2-1.0}-expressing neurons (n = 75 ROIs from 1 culture) with the corresponding EC₅₀ value.
- (J) Representative fluorescence images showing expression and fluorescence response to 10 μM PGD₂ in cultured neurons expressing GRAB_{PGD2-1.0}. The inset in the saline group (left) is contrast-enhanced to show the expression of GRAB_{PGD2-1.0}.
- (K) Summary of the normalized fluorescence responses to the indicated compounds (including PGs and other signaling lipids, each at 10 μM; n = 41 ROIs from 1 culture) in GRAB_{PGD2-1.0} expressing neurons.
- (L) Fluorescence response measured in neurons (n = 30 ROIs from each culture, 3 cultures each) expressing GRAB_{PGD2-1.0} with the indicated concentrations (v/v) of brain homogenate sampled from SD24h and Con mice, followed by 1 μM asapirant.
- (M) Representative fluorescence images showing expression and fluorescence response to 5% SD24 BH in cultured neurons expressing GRAB_{PGD2-1.0}.
- (N) Optimization steps for GRAB_{PGD2-1.1} and the fluorescence responses to 1 μM PGD₂, compared with GRAB_{PGD2-1.0} (dashed line).
- (O) Experimental schematic for *in vivo* GRAB_{PGD2-1.1} recording in POA.
- (P) Representative fluorescence image of the optical fiber implanted mice with GRAB_{PGD2-1.1} virus injected in POA. White dashed area shows the POA, and the white triangle shows the position of the tip of the implanted optical fiber.
- (Q) Immunoblotting of brain lysates from Rosa-Cas9 mice injected with AAV-sgRNA^{Ptgds} (ABC-*Ptgds*^{KO}) or AAV-sgRNA^{NT} (ABC-NT).
- (R) Survival curves for mice (n = 5) induced sepsis by CLP with oral administration of asapirant or vehicle.
- (S) Survival curves for mice (n = 5) induced sepsis by CLP with oral administration of MK-571 in drinking water, compared with water controls.
- (T) Survival curves for *Abcc4*^{-/-} or wild-type mice (n = 5) induced sepsis by CLP.
- Data are presented as means ± SEM. Statistical analysis was performed using two-tailed unpaired t test (A, C, F, and K), one-way ANOVA with Dunnett correction test (B and E), log-rank test (D and R–T), or two-tailed paired t test (L). ns, not significant; *p < 0.05; ***p < 0.001.